CFD Simulations of Superorbital Reentry for a Phobos Sample Return Capsule

Marta Fernandes Pereira Bruxelas

Thesis to obtain the Master of Science Degree in

Aerospace Engineering

Supervisors: Prof. Mário António Prazeres Lino da Silva
Prof. Paulo Jorge Soares Gil

Examination Committee

Chairperson: Prof. Fernando José Parracho Lau
Supervisor: Prof. Mário António Prazeres Lino da Silva
Member of the Committee: Prof. Luís Paulo da Mota Capitão Lemos Alves

November 2017

Acknowledgments

There are many people I would like to thank for helping me during the development of this thesis.

First and foremost, I would like to thank Professor Mário Lino da Silva for accepting to be my supervisor and introducing me to the incredible field of high-temperature gas-dynamics. His guidance and help were indispensable for the success of this work. I thank Professor Paulo Gil for also accepting to be my supervisor and for his advice. I would also like to thank Dr. Maria Castela for answering my late-night e-mails, for introducing me to Inkscape and especially for her willingness to help me during these past few months. Furthermore, I would like to thank Dr. Bruno Lopez, for all the support regarding software SPARK and his readiness to help me.

I gratefully acknowledge company Spin.works for their work in project DIVER, especially Tiago Hormigo for answering all my questions.

I thank all my friends for their company and support. Last but not least, I would like to thank my family. You helped me and supported me through all the difficult and happy times. Your encouragement has been invaluable to me.

Resumo

A reentrada de uma cápsula espacial (de geometria semelhante à cápsula Hayabusa) é simulada para uma missão de recolha de amostras de Phobos (Phobos Sample Return), lua de Marte. A velocidade inicial de reentrada é de 11.6 km/s e a simulação é realizada utilizando o código SPARK, desenvolvido e mantido no IPFN. Os fluxos de calor na superfície da cápsula são calculados para vários pontos de trajectória centrados no pico de calor convectivo, pois o cálculo dos fluxos de calor totais é determinante para o design de um sistema de protecção térmica apropriado. Os processos de geração e de convergência de uma malha computacional são apresentados. Dois modelos para o cálculo de coeficientes de transporte são considerados, o modelo Wilke e o modelo Gupta-Yos, e os resultados obtidos comparados. Para uma análise mais profunda, os resultados são também comparados com simulações previamente realizadas utilizando o mesmo software, mas considerando a cápsula RAM-C II e uma reentrada com velocidade de 7.65 km/s. Os resultados obtidos para os dois modelos são mais semelhantes para uma velocidade de reentrada menor. Uma simulação é realizada aplicando o modelo de duas temperaturas de Park para avaliar o grau de desequilíbrio térmico do fluído. Duas trajectórias são consideradas para a descida da cápsula no âmbito do projecto DIVER. O fluxo de calor convectivo no ponto de estagnação é avaliado para seis pontos de cada trajectória e posteriormente comparado com a relação semi-empírica de Sutton-Graves.

Keywords: Reentrada, Hipersónico, Aerotermodinâmica, Fluxos de Calor Convectivos

Abstract

A simulation of the reentry flow for a Phobos Sample Return Mission is presented. The initial reentry velocity considered is 11.6 km/s and the capsule has the same forward body geometry as the Hayabusa capsule. The simulations are performed using CFD code SPARK, developed and maintained at IPFN. The heat fluxes along the capsule surface are analysed for several trajectory points, centered in the convective heating peak trajectory point, since the assessment of the total heat fluxes is paramount for the proper design of a TPS. A mesh generation process and mesh convergence study are presented. Two methods for calculating the transport properties, Wilke and Gupta-Yos, are applied and compared. The obtained results are also compared against a previous simulation performed using the same software considering the RAM-C II capsule reentry at 7.65 km/s. For the highest reentry speed, both models diverge more than for the lowest speed. An analysis of thermal nonequilibrium is performed applying Park's two-temperature model to account for thermal nonequilibrium and compared against thermal equilibrium conditions. Two trajectories for the capsule descent are considered in the scope of project DIVER, a steep and a shallow entry. The stagnation point convective heat flux is analysed at six key points for each trajectory and compared to the Sutton-Graves semi-empirical correlation used in the preliminary design.

Keywords: Reentry, Hypersonic, Aerothermodynamics, Convective Heat Fluxes

Contents

List of Tables

List of Figures

Nomenclature

Greek symbols

$[\tau]$	Viscous stress tensor.
$\dot{\Omega}$	Thermal energy source term.
$\dot{\omega}$	Species source term.
λ	Thermal conductivity.
μ	Viscosity coefficient.
ν	Stoichiometric coefficient.
ν'	Stoichiometric coefficient on the reactant side of the chemical reaction.
ν''	Stoichiometric coefficient on the product side of the chemical reaction.
ρ	Density.
σ	Collision effective cross-section.

Roman symbols

c	Mass fraction.
C_P	Specific heat at constant pressure.
C_V	Specific heat at constant volume.
D	Diffusion coefficient.
ε	Thermal energy.
E	Total energy.
h	Enthalpy.
J	Mass diffusion flux.
K	Heat transfer coefficient.
k_B	Boltzmann constant.

K_n	Knudsen number.
K_f	Rate constant for the forward process of the chemical reaction.
K_b	Rate constant for the backward process of the chemical reaction.
L	Characteristic dimension of the body.
M	Molar mass.
m	Mass of species.
NS	Total number of species.
p	Pressure.
$\dot{q}_R$	Radiative heat flux.
$\dot{q}_{cond}$	Convective heat flux.
q_C	Conduction heat flux.
R	Specific gas constant.
r_n	Hemispherical nose radius.
T	Temperature.
T_c	Controlling temperature.
u	Mean flow velocity.
V	Mean freestream total velocity.
x	Concentration of species.

Subscripts

i	ith species.
j	jth species.
k	kth energy mode.
r	rth chemical reaction.
e	Refers to the electrons.
exc	Refers to the electronic excitation energy mode.
ion	Refers to the ions.
m	Refers to the molecules.
rot	Refers to the rotational energy mode.

tr	Refers to the translational energy mode.
vib	Refers to the vibrational energy mode.

Superscripts

a	Refers to the ambipolar diffusion.
T	Transpose.

Glossary

CFD	Computational Fluid Dynamics is a branch of fluid mechanics that uses numerical methods and algorithms to solve problems that involve fluid flows.
DIVER	Desenho Integrado de VEículo de Reentrada is a project developed by company Spin.Works in cooperations with company INEGI and research unit IPFN. It concerns all the concurrent engineering required for the initial design of a reentry capsule considering the Phobos sample return mission.
DPLR	Data Parallel Line Relaxation is a CFD code for re-entry flow simulations. It is a structured, finite volume code that solves the Navier-Stokes equations set for a chemically reacting flow.
ERC	Earth Return Capsule is the part of the return vehicle that reenters Earth atmosphere. It detaches itself from the ERV right before reentry.
ERV	Earth Return Vehicle is the vehicle that is used to return to Earth in a Space mission.
ESA	European Space Agency is an intergovernmental organisation dedicated to the exploration of space.
ESTHER	European Shock-Tube for High Enthalpy Research is a shock-tube facility in Lisbon (Portugal) that was developed under the funding of the European Space Agency.
FIAT	Fully Implicit Ablatioon and Thermal Analysis is a code developed by NASA that calculates the surface material response.

FIRE	Flight Investigation of the Reentry Environment was a mission with the purpose of measuring radiative heat transfer at lunar return velocities.
IPFN	Instituto de Plasmas e Fusão Nuclear is a research institute at Instituto Superior Técnico, Lisbon.
LAURA	Langley Aerothermodynamic Upwind Relaxation Algorithm is a structured, finite volume CFD code that solves the Navier-Stokes equations set for a chemically reacting flow.
LEMANS	Le Michigan Aerothermodynamics Navier-Stokes Solver is an unstructured, finite volume CFD code that solves the Navier-Stokes equations for a chemically reacting flow.
MSR	Mars Sample Return mission aims to collect samples from Mars surface and returning them to Earth.
SPARK	Software Package for Aerodynamics Radiation and Kinetics is a CFD code developed and maintained at IPFN. It is a structured, finite volume code that solves the Navier-Stokes equations for a chemically reacting flow.
TPS	Thermal Protection System is the shield that protects the capsule against the intense heat fluxes experienced during reentry.

Chapter 1

Introduction

Robotic planetary exploration missions rank among the most challenging endeavours in Space engineering. Almost every stage of the mission (take-off, cruise, entry, descent, landing, in-situ exploration) is filled with critical obstacles that may jeopardize the entire mission if they are not properly addressed. Space is an unforgiving environment and even the slightest error may lead to the failure of a multi-billion euro mission after years, if not decades of preparation. This was the case recently for the EXOMARS mission, where a small software bug ultimately led to the demise of the exploration vehicle, which crashed on the surface of Mars at several hundred kilometres per hour. The need for Europe to achieve full technological independence in the access to Space - and even more so regarding planetary exploration science - is what led research teams to propose the Phobos Sample Return mission. For almost two decades, a Mars Sample Return (MSR) mission has been in the early stages of planning [1] [2] [3], aiming at collecting and returning samples from the surface of Mars[1] in search of the geological (and possible biological) past of this planet. This mission relies on several key technologies that are not yet mature at European level (as the recent demise of EXOMARS proves) and the Phobos Sample Return mission has been proposed as a stopgap mission to test and validate technological solutions for the future MSR misson, while at the same time avoiding some of its critical issues, such as EDL on Mars, take-off and orbital insertion of a rocket with the collected Mars samples. This mission would also scientifically contribute to Mars exploration since it is postulated that the geological samples from Phobos would in fact be very similar to the ones on Mars.

Figure 1.1 shows the baseline mission architecture for the Phobos Sample Return mission, which is composed of six main stages. The first stage consists in the launch and direct entry into Mars' transfer orbit, using the Proton-M launcher and a Breeze-M upper stage to propel the spacecraft into orbit. The second stage is the Earth-Mars transfer. The third stage consists in descent, landing and surface operations at Phobos surface. Afterwards, stage four is the ascent by ERV (Earth Return Vehicle) and entry into Earth's transfer orbit. Stage five is the Mars-Earth transfer. Finally stage 6 is reentry with ERC (Earth Return Capsule).

One of this mission's most critical technologies is the one behind the superorbital Earth reentry

---

[1] Actually just below the surface, which is irradiated by the Vacuum Ultra-Violet (VUV) radiation from the sun.

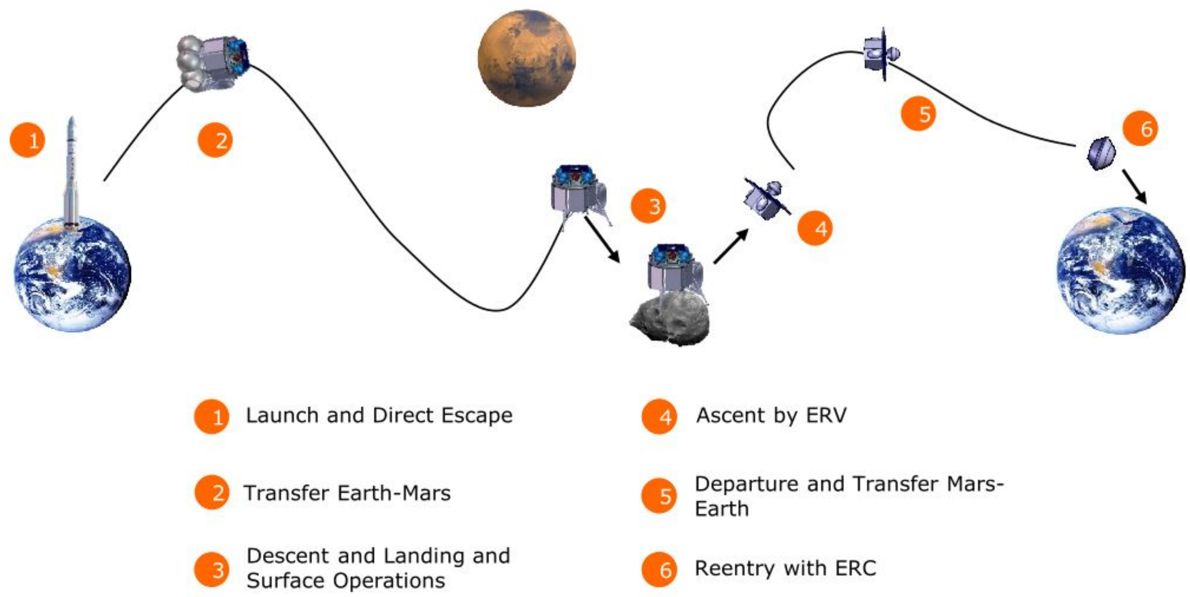

Figure 1.1: Phobos Sample Return baseline mission architecture. Adapted from [4].

originating from Mars/Phobos. At this stage, the spacecraft is moving at superorbital or near-orbital velocities, ranging from 6 to 13 km/s, reaching hypersonic flow conditions. These velocities are much higher than the speed of sound and therefore the flow is hypersonic, which means that the internal energy of the flow is small when compared to its kinetic energy [5]. This leads to the formation of strong and high-temperature shock waves around the capsule.

Figure 1.2 shows a schematic representation of a typical capsule shape and the shock wave formed around it. At the shock, the decrease in the gas kinetic energy balances with the increase in its internal energy, abruptly rising the gas temperature to values around 10^4 to 10^5 K order of magnitude. Because of these high temperatures, the gas is highly reactive. Among other processes, the endothermic reactions inside the shock layer (*see* Fig. 1.2), will help the gas cool down before interacting with the capsule surface. This is the main reason why the capsule has a forward blunt-shaped design. This blunt shape is designed so that the detached bow shock is at a distance δ_3 (*see* Fig. 1.2) large enough from the capsule surface to allow efficient radiative and convective cooling processes to occur inside the boundary layer. If the gas cooling is ensured, the Thermal Protection System can withstand the heat fluxes at the capsule surface. An accurate assessment of these heat fluxes during the high speed, hyperbolic reentry is, therefore, critical to the overall spacecraft design.

These heat fluxes that reach the capsule wall can be divided into two types, convective heat flux and radiative heat flux. The convective heat flux refers to the energy transfered by particles colliding and interacting with the surface. It is composed of a conduction component (determined by the temperature gradient) and a diffusive component (determined by the mole fraction gradient). The radiative heat flux is sourced in the radiation emitted by the excited particles. In flows at superorbital velocities, the radiative heat load can be significantly higher than the convective heating [6]. Moreover, which heat flux is dominant can also be related to the capsule's geometry, since radiative heating is proportional to the shock layer thickness, which increases as the body diameter increases [7]. As an example, for

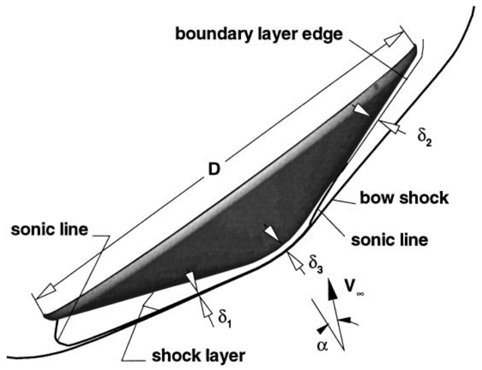

Figure 1.2: Detached bow shock formed around a blunt shaped nose capsule. δ_3 represents the shock stand-off distance. Adapted from [7].

the Galileo Probe, a capsule that entered Jupiter's atmosphere in 1995, heating was mostly by radiation [8], whereas for the Stardust mission, a capsule with a smaller diameter, the dominant heat flux was the convective one [9]. Since the geometry considered in the present work is very similar to the Stardust geometry, a greater emphasis will be given to the calculation of the convective heat fluxes at the surface. In addition to the ionization and dissociation processes occuring in the flow, recombination reactions may take place at the capsule's surface depending on its material. These result from the interaction between the colliding flow particles with the surface. The latter serves as a catalyst for these exothermic reactions, greatly increasing the heat flux at the surface [10]. Consequently, all these processes must be taken into account when performing these simulations, which makes this one of the greatest challenges of designing a Space return mission.

1.1 Project DIVER

DIVER (Desenho Integrado de VEículo de Reentrada) is a Portuguese consortium project comprising Spin.works, INEGI (Instituto de Ciência e Inovação em Engenharia Mecânica e Engenharia Industrial), IST-DEM and IPFN (Instituto de Plasmas e Fusão Nuclear), funded by Portugal2020. It gathers all the concurrent engineering required in the preliminary design of a reentry vehicle in the Phobos Sample Return mission and aims at demonstrating national expertise on interplanetary exploration missions design. Two trajectories for the capsule descent are considered, one with a flight path angle (fpa) of -15.9°, Trajectory 15.9, and the other with fpa = -24.2°, Trajectory 24.2. In both trajectories, the maximum value of the reentry velocity is 11.6 km/s.

1.2 Objectives

The purpose of this thesis is to:

- Identify the key trajectory points for the proper design of the capsule.
- Calculate the convective heat fluxes for each trajectory key points.

- Provide a first estimate of the heat fluxes for the next phase of the design.

In order to accomplish these objectives, CFD simulations will be performed. They will consider two different transport models (Wilke and Gupta-Yos). A one-temperature model and a multi-temperature model will be considered to account for thermal equilibrium and nonequilibrium conditions. The software tool SPARK will be used. It is a hypersonic CFD code developed and maintained by IPFN. There were more objectives to this thesis, however, due to the time required until convergence, they were not achieved and hence are merely discussed in the conclusion section.

1.3 State-of-the-art

There are three approaches to study the reentry flowfield around a capsule: flight testing, ground testing and numerical simulations. Flight testing a capsule before each mission would be very expensive, time consuming and not viable at all. The reentry environment is characterized by a high enthalpy and low density flow, making it difficult to mimic these conditions on the ground/experimentally. As a result, numerical simulations are still a powerful tool to understand and efficiently design reentry capsules. Nevertheless, this kind of simulations are challenging, especially to fully capture the multi-physics phenomena.

As explained before, the gas is highly reactive in the shock layer. To accurately model a hypersonic reentry, a large number of complex gas dynamics processes must be taken into account, such as molecular collisions leading to dissociation/recombination and/or ionization of molecules and/or atoms, charged particle interactions, and radiation [11]. The modelling of these phenomena often requires empirical parameters that can be obtained from simple, yet accurate, experimental studies in ground facilities. Ground test facilities such as shock tubes, arc-jets and plasma torches are designed to generate high enthalpy flows in order to obtained these empirical parameters. An example of this kind of facilities is the ESTHER (European Shock-Tube for High Enthalpy Research) shock tube [12], which will simulate spacecraft atmosphere reentry conditions by generating a shock wave through the deflagration of a hydrogen, oxygen and helium gas mixture. For many years now, there has been a number of experiments performed and the resulting data analysed. Hanson and Baganoff [13] analysed several shock tube data to obtain the collision dissociation rates for nitrogen. Park [14] re-interpreted experimental data on dissociation of nitrogen and oxygen, from shock tube tests, using a two-temperature thermo-chemical model to determine the rate coefficients consistent with the model.

Due to the complexity of simulating these conditions experimentally, numerical simulations are the most economical approach to study this environment. These simulations are very complex and computationally expensive and hence not many people have the resources to perform them. Despite the fact that engineering models can hold a first estimate of the aerodynamic coefficients and the heat fluxes on the forward body, detailed numerical simulations are used to provide a better understanding of the physical phenomena. The physical models that have been developed based on theory and experimental data are implemented on a computational solver that will perform numerical simulations. Moreover, these numerical simulations and physical models can be verified and validated by comparing the numerical results against the experimental tests and flight data, when available. The following numerical simulations have been performed after or before their official mission, with the purpose of designing a TPS or validating models, respectively, and have considered a reentry velocity similar to the one in this work.

Stardust Mission. A mission to retrieve samples of interstellar dust from the tail of comet Wild-2. The reentry velocity of this capsule was 12.8 km/s and Trumble et al [15] analysed it using the CFD code DPLR (Data Parallel Line Relaxation), coupled with the FIAT code (Fully Implicit Ablation and Thermal Analysis) for the surface material response. This analysis considered a 2D axisymmetric computational domain of the full capsule geometry and was performed on 21 points along the trajectory. Mitcheltree et al. [16] used the software tool LAURA (Langley Aerothermodynamics Upwind Relaxation Algorithm) to perform numerical simulations at nine trajectory points in the hypersonic regime. LAURA solver uses an upwind-biased, point-implicit relation algorithm for solving the Navier-Stokes equations for 3D viscous, hypersonic flows in thermochemical nonequilibrium. The numerical results were in good agreement with the Newtonian fluid approximation. Alkandry et al. [17] analysed the impact of different transport models on the numerical results. For a maximum freestream velocity of 12.1 km/s, the Gupta-Yos and Wilke transport models were considered together with the chemistry model composed by 19 species and catalytic boundary conditions to account for ablation. The results have shown that both models agreed well at low velocities whereas at high velocities, the wall heat flux predicted by the Wilke model was higher than the one obtained using the Gupta-Yos model.

Hayabusa Mission. A mission to retrieve samples from the Itokawa asteroid. The capsule's reentry velocity was 11.7 km/s and Fahy et al. [18] used the eilmer3 code, developed in the University of Queensland, to perform the CFD simulations of the reentry conditions. eilmer3 solves the integral form of the Navier-Stokes equations and discretizes the computational domain using the cell-centered finite volume method for 2D or 3D simulations. Park's 21 reaction scheme with 11 species was used for the kinetic model, where thermal nonequilibrium was taken into account by Park's two-temperature model. Viscous transport properties were modelled by the Gupta-Yos model. A super-catalytic wall boundary condition was considered, although it had little overall effect on the flow aerothermal dynamics. There was good agreement between the numerical data and flight data.

Fire II Mission. FIRE (Flight Investigation of the Reentry Environment) II was a mission with the purpose of measuring radiative heat transfer at lunar return velocities in a non-ablating environment. The capsule reentered Earth's atmosphere at 11.4 km/s and Lopez and Lino da Silva [19] performed a CFD analysis of a single reentry trajectory point using code SPARK. An 11 species air model and a multi-temperature model were considered. Scalabrin and Boyd [20] performed a numerical simulation of the convective and radiative heating rates using code LEMANS. LEMANS is a Navier-Stokes solver that uses a finite-volume method in a unstructured mesh. The species mass production rates were modelled using a standard finite-rate chemistry model for reacting air in conjuction with Parks's two-temperature model. Two different models for transport properties are compared, Wilke and Gupta-Yos as well as two surface boundary conditions, catalytic and noncatalytic. The results agreed well with simulations using codes DPLR and LAURA, routinely used in reentry calculations.

Apollo Missions. Park [21] performed numerical simulations for the Apollo 4 mission, in order to calculate the stagnation point radiation heating rate. Simulations at three points in time were considered, with a maximum velocity of 10.5 km/s. A noncatalytic wall boundary condition was considered for the recombination of O and N, as well as a viscous shock layer method to account for ablation. A kinetic scheme considering 20 species was considered, together with a two-temperature model. The value obtained for the convective heating in the absence of radiation was lower when compared to the Fay–Riddell correlation, however, this difference was attributed to the effect of blowing.

Generic Sample Return Mission. Carandente et al. [22] performed an aerothermal analysis of a capsule reentering Earth from an interplanetary exploration mission at 13.1 km/s. A solution of the Navier-Stokes equations was computed for a chemically reacting air mixture composed of 11 species. Numerical simulations were performed using software tool FLUENT, which is able to solve the laminar Navier-Stokes equations at high temperatures in chemical nonequilibrium, including dissociation and ionization reactions. Furthermore, the AUSM (Advanced Upstream Splitting Method) scheme for convective numerical fluxes was employed. A catalytic surface was considered and the results compared to the ones obtained applying a noncatalytic surface boundary condition. It was observed that the Sutton-Graves equation for convective heat fluxes predicted a lower stagnation point heat flux when compared to the results obtained assuming a catalytic wall boundary conditions.

Based on the presented studies, one can see that there is a large number of different physical models and correlations currently applied in CFD codes in order to simulate reentry conditions. All have been extensively studied and numerically validated, however not all numerical data obtained agreed well with either experimental data or flight data. This leads to the conclusion that despite the proved success of some models and correlations in properly defining the processes at reentry, there are still opportunities for further development in this area.

1.4 Thesis Outline

This work is divided into five main chapters, of which the present one constitutes the introduction, state-of-the-art and goals of this master thesis.

Chapter 2 presents and describes the problem's governing equations, as well as all the physical models.

Chapter 3 presents the numerical setup. It comprises all the simulation parameters and inputs considered during the computational simulations. It also describes the strategies that were applied in order to reach convergence of the problem.

Chapter 4 shows and discusses the numerical results.

Finally, Chapter 5 presents the conclusions and future work.

Chapter 2

Governing Equations and Physical Models

In order to perform a CFD simulation, the problem at hand must first be theoretically formulated. For a reentry environment simulation, there are a lot of considerations and physical models that need to be taken into account.

To accurately describe this environment, the conservation equations for a thermal nonequilibrium reactive flow are presented in section 2.2. In this formulation, there are still some properties that require further description. To this effect, an explanation of a chemical-kinetic model and a multi-temperature model are detailed in sections 2.3 and 2.4, respectively. Moreover, in order to model the transport properties, section 2.5 introduces the underlying physical models considered, as well as two distinct methods to calculate the transport coefficients. There is the Wilke/Blottner/Eucken Model (described in section 2.5.1) and the Gupta-Yos/Collision Cross-Section Model (detailed in section 2.5.2). Ambipolar diffusion is presented and detailed in sections 2.5.3.

2.1 Thermal Nonequilibrium Reacting Flow

A reacting flow is described by a multi-component model. This means the gas is treated as a mixture of individual chemical species, mixed in a single phase. Consequently the gas properties are represented by bulk properties as a function of the local chemical composition.

A gas is in chemical nonequilibrium when the characteristic time of a fluid element is lower than that of the chemical reactions and vibrational excitation [23]. For a reentry capsule at superorbital velocities, the collisions taking place in the shock layer are not instantaneous, they have an associated time. This time is greater than the characteristic time of the flow, which means that even in steady state flow conditions, the chemical composition of the flow may have not yet reached chemical equilibrium. Consequently, the gas composition cannot be modelled only as a function of the gas state variables and a chemical-kinetic model need to be applied. This model adds a mass conservation equation for each species (eq. 2.1) to the conservation equations.

As previously stated, during reentry the massive amount of kinetic energy in the hypersonic freestream is converted into internal energy of the gas across the strong bow shock wave. This transfer from kinetic energy to internal energy occurs through excitation of the molecules' modes of energy. Depending on the nature of the molecule (monoatomic, diatomic or polyatomic), the degrees of freedom vary (3,5 and 6 respectively). These degrees of freedom are associated to four main thermal energy modes: translational energy ε_{tra} , rotational energy ε_{rot}, vibrational energy ε_{vib} and electronic excitation energy ε_{exc} [23]. Figure 2.1 shows a graphical representation of all four thermal energy modes.

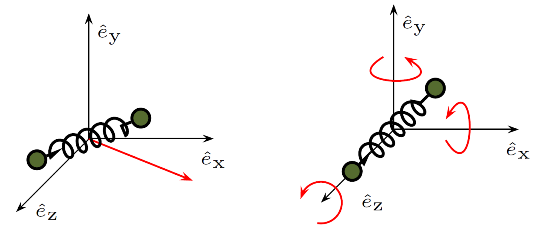

(a) Translational Mode (b) Rotational Mode

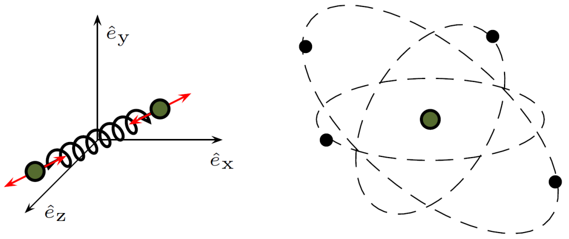

(c) Vibrational Mode (d) Electronic Excitation Mode

Figure 2.1: Graphical representation of the energy modes. Adapted from [24].

These thermal energies, as the name suggests, are a function of their corresponding temperatures. Considering thermal equilibrium, every species thermal energy is associated to the same temperature $T = T_{\text{tr}} = T_{\text{rot}} = T_{\text{vib}} = T_{\text{exc}}$. However, usually species thermal energy modes are excited differently and thus, multiple temperatures must be considered. Equilibrium is only reached after energy exchanges take place, with each exchange having an associated relaxation time. If these times are greater than the characteristic time of the flow, the flow is in thermal nonequilibrium. To account for this, a multi-temperature model must be devised and an extra equation for the conservation of the global thermal energy ε_k of each thermal energy mode has to be considered (eq. 2.4).

2.2 Conservation Equations

Equations (2.1 - 2.4) present the conservation equations for a thermal nonequilibrium reacting flow. The species continuity equation (eq. 2.1) establishes the conservation of each species, accounting for the production and destruction of species in the source term $\dot{\omega}_i$, based on the local state of the flow and the characteristic time scale defined for each reaction. The momentum equation (eq. 2.2) enforces Newton's Second Law. The total energy equation (eq. 2.3) constitutes the conservation of energy. The thermal nonequilibrium energy equation (2.4) ensures conservation of the global thermal energy of each thermal energy mode.

$$\frac{\partial(\rho c_i)}{\partial t} + \vec{\nabla} \cdot (\rho c_i \vec{u}) = \vec{\nabla} \cdot \vec{J}_i + \dot{\omega}_i \tag{2.1}$$

$$\frac{\partial(\rho \vec{u})}{\partial t} + \vec{\nabla} \cdot (\rho \vec{u} \otimes \vec{u}) = \vec{\nabla} \cdot [\tau] - \vec{\nabla} p \tag{2.2}$$

$$\frac{\partial(\rho E)}{\partial t} + \vec{\nabla} \cdot (\rho E \vec{u}) = \vec{\nabla} \cdot \left(\sum_k \vec{q}_{C_k} + \sum_i \vec{J}_i h_i + \vec{u} \cdot [\tau] - p\vec{u} \right) \tag{2.3}$$

$$\frac{\partial}{\partial t}(\rho \varepsilon_k) + \vec{\nabla} \cdot (\rho \vec{u} h_k) = \vec{\nabla} \cdot \left(q\vec{_{C_k}} + \sum_i \vec{J}_i h_{i,k} \right) + \dot{\Omega}_k \tag{2.4}$$

where ρ is the density, $\vec{u}$ the mean velocity in vectorial form, c_i the species i mass fraction, $\vec{J}_i$ the species i mass diffusion flux, $\dot{\omega}_i$ the species i source term, $[\tau]$ the viscous stress tensor, p the pressure, E the total energy, $\vec{q}_{C_k}$ the conduction heat flux, h the enthalpy of the flow, ε_k the global thermal energy of the kth thermal energy mode and $\dot{\Omega}_k$ the thermal energy source term.

2.3 Kinetic Model

In the above stated equation for the species continuity (eq. 2.1), there is an unspecified parameter $\dot{\omega}_i$. This is a source term that is determined by a chemical-kinetic model, since the number of reactions to describe a specific flow is not fixed (depending on the kinetic scheme considered the number of chemical reactions and their respective rates are different). The kinetic scheme considered in this work is the 11 species air model considered by Park [25]. It considers the species O_2, N_2, NO, N, O, N_2^+, O_2^+, NO^+, N^+, O^+, e^-.

The kinetic source term reads [26]:

$$\dot{\omega}_i = M_i \sum_r \Delta\nu_{ir} \left[K_{\mathsf{f}_r} \prod_i {x_i}^{\nu'_{ir}} - K_{\mathsf{b}_r} \prod_i {x_i}^{\nu''_{ir}} \right] \tag{2.5}$$

where ν'_{ir} and ν''_{ir} are the reactant and product stoichiometric coefficients, respectively, $\Delta\nu_{ir} = \nu''_{ir} - \nu'_{ir}$, and $x_i = \rho_i/M_i$ is the concentration of species i. The rate constants K_{f_r} and K_{b_r} are related to the forward and backward processes of the r reaction.

2.4 Multi-Temperature Model

A multi-temperature model is introduced to establish the total temperature dependence of the energy stored in each energy mode. It further defines the source term $\dot{\Omega}_k$ ([27],[28]), present in equation 2.4, that characterizes the energy exchange between the different energy modes. Moreover, the model establishes the link between each species thermal energy and the global thermal energy to be:

$$\varepsilon_k = \sum_i c_i \varepsilon_{k,i} \tag{2.6}$$

where $\varepsilon_{k,i}$ stands for each species thermal energy of each thermal energy mode.

In SPARK, the two-temperature model by Park [29] is implemented, which considers, as the name suggests, two temperatures. The first, temperature T_{tr}, characterizes the translational energy of the atoms and molecules. The second one is T_{vib}, the temperature that characterizes the vibrational energy of the molecules. The model further assumes that the rotational mode of the molecules is in equilibrium with the translational mode ($T_{\text{tr}} = T_{\text{rot}}$) and that the translational energy mode of the electrons and electronic excitation energy mode of atoms and molecules are in equilibrium with the vibrational mode ($T_{\text{vib}} = T_{\text{e}} = T_{\text{exc}}$). This is a reasonable assumption for the conditions of an atmospheric reentry ([27],[28]).

This model calculates molecular constants using the Millikan and White [30] linear relation between the vibrational relaxation times and the constants to be determined. This method further considers that all interactions occur at the same distance and it does not take into account the rotational energy, should the collisions involve a diatomic molecule.

2.5 Transport Models

During a hypersonic flight, ionization and dissociation of the flow molecules take place downstream of the shock wave. Ionization causes a change in the high-temperature gas mixture transport property, because it introduces electrical conductivity and ambipolar diffusion (explained in section 2.5.3) into the flow medium, which now consists of a plasma [31]. Consequently, determining the flow transport properties is required.

In the conservation equations previously stated (eqs. 2.1 - 2.4), $\vec{J}_i$, $[\tau]$ and $\vec{q}_{C_k}$ define the dissipative fluxes and are usually a function of their respective transport coefficient and gradient. Table 2.1 lists all the dissipative fluxes and their respective transport coefficient and gradient.

Table 2.1: Dissipative fluxes and corresponding transport coefficients and gradients. Presented in S.I. units.

	Dissipative Flux		Transport Coefficient		Gradient	
Mass Diffusion	$\vec{J}_i$	kg·m^{-2} · s^{-1}	D_i	m^2 · s^{-1}	$\vec{\nabla}(c_i)$	m^{-1}
Viscosity	$[\tau]$	N·m^{-2}	μ	kg·m^{-1} · s^{-1}	$\vec{\nabla} \cdot \vec{u}$	s^{-1}
Thermal Conductivity	$\vec{q}_{C_k}$	J·m^{-2} · s^{-1}	λ_k	J·s^{-1} · m^{-1} · K^{-1}	$\vec{\nabla} T_k$	K ·m^{-1}

It is considered that the mass diffusion flux $\vec{J}_i$ is as described by Fick's Law of diffusion:

$$\vec{J}_i = \rho D_i \vec{\nabla}(c_i) \tag{2.7}$$

where D_i represents the ith species mass diffusion coefficient.

Moreover, it is considered that the viscous stress tensor $[\tau]$ assumes a Newtonian fluid and the Stokes hypothesis for the normal stresses:

$$[\tau] = \mu\left(\vec{\nabla}\vec{u} + (\vec{\nabla}\vec{u})^T\right) - \frac{3}{2}\mu(\vec{\nabla}\cdot\vec{u})[I] \tag{2.8}$$

where μ is the viscosity coefficient.

Furthermore, the conduction heat flux for each thermal energy mode, $\vec{q}_{C_k}$, is assumed to be given by Fourier's Law of heat conduction:

$$\vec{q}_{C_k} = \lambda_k \vec{\nabla} T_k \tag{2.9}$$

These transport coefficients can be obtained by using the classical Chapman-Enskog solution for the Boltzmann equation system [32]. However, this method requires the solution of a complex system of linear equations thus it is very computationally expensive. The most effective way of determining these properties is by applying approximate mixing rules, simplified forms of the Chapman-Enskog solution.

In this work, two different mixing rules are applied. The first is the Wilke/Blottner/Eucken model (section 2.5.1) and the second one is the Gupta-Yos/Collision Cross-Section model (section 2.5.2).

2.5.1 Wilke/Blottner/Eucken Model

Wilke's Model [33] for gas mixture viscosities was developed through the application of kinetic theory to the first order Chapman-Enskog relation. It assumes that all interactions between any particles present the same (hard sphere) cross-section [34]. The gas mixture viscosity μ and the thermal conductivity λ_k for each global thermal energy mode are determined as follows:

$$\mu = \sum_{i=1}^{NS} \frac{x_i \mu_i}{\phi_i} \qquad\qquad \lambda_k = \sum_{i}^{NS} \frac{x_i \lambda_{k,i}}{\phi_i} \tag{2.10}$$

where x_i is the species molar fraction and μ_i represents the species individual viscosities. ϕ_i is a scale factor given by:

$$\phi_i = \sum_{j=1}^{NS} \left[1 + \sqrt{\frac{\mu_i}{\mu_j}}\left(\frac{M_j}{M_i}\right)^{\frac{1}{4}}\right]^2 \Big/ \sqrt{8\left(1 + \frac{M_j}{M_i}\right)} \tag{2.11}$$

where M_* represents each species' (i or j) molar mass.

For the species viscosities, curve fits determined by Blottner et al. [35] are considered:

$$\mu_i(T_{\text{tra,i}}) = 0.1\text{exp}((A_i \ln T_{\text{tra,i}} + B_i)\ln T_{\text{tra,i}} + C_i) \tag{2.12}$$

where A_i, B_i and C_i are curve fitted coefficients for each species.

Eucken's relation [36] is used to determine each species thermal conductivity for its translational mode $\lambda_{\text{tra},i}$ and for its remaining energy modes $\lambda_{k\neq\text{tra},i}$:

$$\lambda_{\text{tra},i} = \frac{5}{2}\mu_i C_{V_{\text{tra},i}} \qquad\qquad \lambda_{k\neq\text{tra},i} = \mu_i C_{V_{k,i}} \tag{2.13}$$

where $C_{V_{k,i}}$ represents the specific heat at a constant volume of the i species in each energy mode.

In thermal nonequilibrium, the contributions of each species should be accounted for differently in the mixing rule according to the multi-temperature model considered.

The species mass diffusion coefficient is given by a single binary coefficient D assuming a constant Lewis number, Le = 1.2:

$$D_i = D = \frac{\text{Le}\lambda}{\rho C_P} \tag{2.14}$$

where C_P is the gas mixture total specific heat at a constant pressure and λ represents the total thermal conductivity of the gas mixture. The Lewis number Le corresponds to the ratio of the energy transport due to mass diffusion relative to the one due to thermal conduction.

Wilke's model presents accurate results for non-ionized gas mixtures and poor results for an ionized mixture (over 10000 K). It is expected to predict higher heat fluxes at the wall when compared to the Gupta-Yos model at high velocities [17].

2.5.2 Gupta-Yos/Collision Cross-Section Model

Another method to calculate the transport properties of a gas mixture is by using the Gupta-Yos model [37], a simplification of the Chapman-Enskog solution. The main difference between the Wilke model and the Gupta-Yos model is that the latter considers each collision's corresponding cross-section. Therefore, it is assumed to be more accurate because the true nature of the viscosity collision integrals is taken into account. However, it requires reasonably accurate collision integral data for each species pair in the gas mixture and thus it is not possible to implement this model if there is no data available. The collision integrals ${\Delta_{ij}}^{(1)}$ and ${\Delta_{ij}}^{(2)}$ are defined as follows:

$${\Delta_{ij}}^{(1)}(T_c) = \frac{8}{3}\left[\frac{2M_iM_j}{\pi RT(M_i + M_j)}\right]^{1/2} \pi{\overline{\Omega}_{ij}}^{(1,1)} \tag{2.15}$$

$${\Delta_{ij}}^{(2)}(T_c) = \frac{16}{5}\left[\frac{2M_iM_j}{\pi RT(M_i + M_j)}\right]^{1/2} \pi{\overline{\Omega}_{ij}}^{(2,2)} \tag{2.16}$$

where ${\overline{\Omega}_{ij}}^{(1,1)}$ and ${\overline{\Omega}_{ij}}^{(2,2)}$ represent weighted averages of the cross-sections, which are evaluated as curve fits to the tabular data generated in [38].

The collision integrals considered in this model's formulation are a function of the controlling temperature T_c that varies depending on the type of particles colliding. For collisions between heavy-particles, the controlling temperature is the translational/rotational temperature (T_{tr}), whereas the one for collisions involving electrons is the vibrational/electron/electronic excitation temperature (T_{vib}) [17].

For the calculation of the gas mixture viscosity, the following equation is used:

$$\mu^{(1)} = \sum_{i}^{NS} \frac{m_i x_i}{\sum\limits_{j}^{NS} x_j \Delta_{ij}^{(2)}} \tag{2.17}$$

where m_i is the ith species mass. The translational mode of heavy species λ_{tra} and electrons λ_{e} read:

$$\lambda_{\text{tra}} = \frac{15}{4} k_B \sum_{i \neq e} \frac{x_i}{\sum\limits_j \alpha_{i,j} x_j \Delta_{ij}^{(2)}(T_{\text{tr}})} \qquad \lambda_{\text{e}} = \frac{15}{4} k_B \frac{x_e}{\sum\limits_j \alpha_{e,j} x_j \Delta_{ej}^{(2)}(T_{\text{vib}})} \tag{2.18}$$

where k_B is the Boltzmann constant and $\alpha_{i,j}$ is given by:

$$\alpha_{i,j} = 1 + \frac{[1 - M_i/M_j][0.45 - 2.54(M_i/M_j)]}{[1 + (M_i/M_j)]^2} \tag{2.19}$$

The global thermal conductivities associated with the rest of the heavy species energy modes, λ_{rot}, λ_{vib}, λ_{exc} are:

$$\lambda_{\text{rot}} = \sum_{i=m} \frac{x_i m_i C_{V_{\text{rot},i}}}{\sum\limits_j^{NS} x_j \Delta_{ij}^{(1)}} \qquad \lambda_{\text{vib}} = \sum_{i=m} \frac{x_i m_i C_{V_{\text{vib},i}}}{\sum\limits_j^{NS} x_j \Delta_{ij}^{(1)}} \qquad \lambda_{\text{exc}} = \sum_{i=m} \frac{x_i m_i C_{V_{\text{exc},i}}}{\sum\limits_j^{NS} x_j \Delta_{ij}^{(1)}} \tag{2.20}$$

In thermal equilibrium, the total thermal conductivity λ is given by:

$$\lambda = \lambda_{\text{tra}} + \lambda_{\text{e}} + \lambda_{\text{rot}} + \lambda_{\text{vib}} + \lambda_{\text{exc}} \tag{2.21}$$

In thermal nonequilibrium, the thermal conductivity associated with each thermal energy mode is calculated by considering the individual contributions of each species according to the multi-temperature model considered.

The mass diffusion coefficient D_{ij} defines the diffusion velocity of each species relative to the other species and reads:

$$D_{ij} = \frac{k_B T_c}{p \Delta_{ij}^{(1)}} \tag{2.22}$$

An effective diffusion coefficient D_i can be determined by regarding the multi-component mixture as a binary mixture consisting on species i and a composite species that represents the rest of the species. It is determined by:

$$D_i = \frac{1 - x_i}{\sum\limits_{j \neq i} \frac{x_j}{D_{ij}}} \tag{2.23}$$

For a single species, its properties are determined as follows:

$$\mu_i = \frac{5}{16} \frac{\sqrt{\pi m_i k_B T_c}}{\pi \overline{\Omega}_{ij}^{(2,2)}} 10^{20} \tag{2.24}$$

$$\lambda_{\text{tra},i} = \frac{75}{64} k_B \frac{\sqrt{\pi k_B T_c / m_i}}{\pi \overline{\Omega}_{ij}^{(2,2)}} 10^{20} \tag{2.25}$$

$$\lambda_{\text{rot},i=m} = \frac{8}{3} k_B C_{V_{\text{rot},i}} \frac{\sqrt{\pi k_B T_c m_i}}{\pi \overline{\Omega}_{ij}^{(1,1)}} 10^{20} \tag{2.26}$$

$$\lambda_{\text{vib},i=m} = \frac{8}{3} k_B C_{V_{\text{vin},i}} \frac{\sqrt{\pi k_B T_c m_i}}{\pi \overline{\Omega}_{ij}^{(1,1)}} 10^{20} \tag{2.27}$$

$$\lambda_{\text{exc},i\neq e} = \frac{8}{3} k_B C_{V_{\text{exc},i}} \frac{\sqrt{\pi k_B T_c m_i}}{\pi \overline{\Omega}_{ij}^{(1,1)}} 10^{20} \tag{2.28}$$

where μ_i represents the viscosity for one species i, $\lambda_{\text{tra},i}$ the translational thermal conductivity and $\lambda_{\text{rot},i}$, $\lambda_{\text{vib},i}$ and $\lambda_{\text{exc},i}$ represent the internal energy modes thermal conductivity. Consequently, the total thermal conductivity for a single species is:

$$\lambda_i = \lambda_{\text{tra},i} + \lambda_{\text{rot},i} + \lambda_{\text{vib},i} + \lambda_{\text{exc},i} \tag{2.29}$$

This model presents better results for weakly-ionized flow without requiring as much computational effort as the Wilke model. However, the simplifications employed in its formulation will cause poor agreement between the Gupta–Yos model and the multicomponent formulation for significantly ionized flows [34].

2.5.3 Ambipolar Diffusion

In an ionized gas, each charged particle induces an electric field, which influences the other particles motion. This results in an increase in the diffusion of the ions, which are *pulled* by the more mobile electrons, which in turn are slowed down by the heavier ions. The two species finally diffuse with the same velocity, mainly imposed by the heavier species. Since the electro-static forces are not considered in the conservation equations, this phenomena can only be taken into account by artificially introducing this effect in the calculation of the charged particles diffusion. The ambipolar corrections account for this increase in diffusion velocity of ions and decrease in velocity of electrons due to the electrostatic interactions between the two.

For ions, Chen [39] shows that the ambipolar diffusion coefficient is given by:

$$D^a_{\text{ion}} = \big(1 + \frac{T_{\text{e}}}{T_{\text{ion}}}\big) D_{\text{ion}} \tag{2.30}$$

where D_{ion} is the ion free diffusion coefficient and T_{e} and T_{ion} are the translational temperatures of the electrons and the ions, respectively. In thermal equilibirum, this ionic factor is simply equal to 2 ($D^a_{\text{ion}} = 2D_{\text{ion}}$), assuming that all heavy species are in translational equilibrium with a common translational temperature.

For electrons, the ambipolar diffusion coefficient is defined as a weighted sum of the ions ambipolar diffusion coefficient, obtained by equalizing the ion and electron number fluxes in a two-species mixture [40]:

$$D^a_{\text{e}} = M_{\text{e}} \frac{\sum_{i=ion} D^a_i x_i}{\sum_{i=ion} M_i x_i} \tag{2.31}$$

This is only valid if all the ions have the same free diffusion velocity and electrical mobility.

Chapter 3

Numerical Setup

After correctly defining the problem, the simulation needs to be set-up. In this section, a short description of the CFD code SPARK is shown in section 3.1. Using semi-empirical correlations, the key trajectory points where the analysis will be performed for project DIVER, corresponding to the initial conditions, are introduced in section 3.2. A mesh generation study is detailed in section 3.3, followed by the mesh convergence study (section 3.3.1). This is a very important part of the simulation setup, because it greatly impacts the results accuracy, as well as the computational effort required. The boundary conditions are detailed in section 3.4, with emphasis on the catalytic boundary condition in section 3.4.1. All the simulation parameters constituting an input in the SPARK code are detailed in section 3.5. Finally, the computational strategy adopted for this problem is descrived in section 3.6.

3.1 SPARK

Software Package for Aerodynamics, Radiation and Kinetics (SPARK) [19] is a CFD code for the simulation of hypersonic nonequilibrium flows. It is a multidimensional (0D up to 2D), second-order finite volume method discretization solver for Navier-Stokes and reactive flow governing equations in structured meshes.

It is written in Fortran 03/08 and explores the newly supported object-oriented feature, enabling the encapsulation of different physical models, numerical methods, mesh related operations and interface communications. Two thermodynamic models are implemented in SPARK: multi-temperature and state-specific kinetic models.

The system is marched in time towards convergence. At each time iteration, a loop over all mesh blocks is done in which the convective fluxes, the dissipative fluxes and the nonequilibrium source terms are computed.

3.2 Selection of the Key Trajectory Points

This thesis' role in the DIVER project is to calculate the heat fluxes present at the wall so that a suitable TPS can be sized. Two separate trajectories were considered, and for each of these trajectories, semi-empirical correlations were applied as a first approach.

For the convective heating, the Sutton-Graves relation [41] was applied. It is a general equation for the stagnation point convective heating to an axisymmetric blunt body for gases in chemical equilibrium, formulated as a function of the mass fraction, molecular weight and transport parameter of the base gases. The Sutton-Graves relation for Earth reentry reads:

$$\dot{q}_{conv} = K\sqrt{\frac{\rho}{r_n}}V^3 \tag{3.1}$$

where K is the heat transfer coefficient and K = 1.7415x10^{-4} for an Earth entry, r_n the hemispherical nose radius and V the freestream velocity.

To analyse radiative heating, the expression developed by Tauber and Sutton [42] was considered. It assumes thermochemical equilibrium and considers only the ”cold-wall” heating that occurs in the absence of ablation. The expression is given by:

$$\dot{q}_R = C{r_n}^a \rho^b f(V) \tag{3.2}$$

where C is a constant that for Earth reentry is C = 4.736x10^4 and $f(V)$ are tabulated values in [42] that are functions of the flight velocity V and the atmospheric composition. b is a constant that equals 1.22 for an Earth entry and a is a function of the density and velocity that reads:

$$a = 1.072\text{x}10^6 V^{-1.88} \rho^{-0.325} \tag{3.3}$$

The trajectory data has been calculated by Spin.works and supplied to IPFN. Figure 3.1 shows the results obtained for the convective (dark blue line) and radiative (light blue line) heat fluxes, the drag (dark red line) and velocity (light red line) distributions during reentry and the points where the analysis will be performed (green dashed line) for (a) Trajectory 15.9 and (b) Trajectory 24.2.

Six points per trajectory were selected to perform the simulations, a standard procedure when performing a CFD analysis. The most critical point, point 3, corresponds to peak heating (peak in convective heat flux). The second most critical, point 5, is the peak in drag (peak in dynamic pressure) because it is the point where the dynamical loads are at their peak. Points 1, 2, 4 and 6 are chosen as points where both convective heating and drag effects are not as dominant, in order to ascertain the correlations accuracy when compared to the simulation data. Tables 3.1 and 3.2 show the selected points data for Trajectory 15.9 and Trajectory 24.2, respectively. The data was calculated considering the US Standard Atmosphere 1976 to model Earth's Atmosphere.

The calculation of the Knudsen number (K_n) is a way to validate the use of the Navier-Stokes formu-

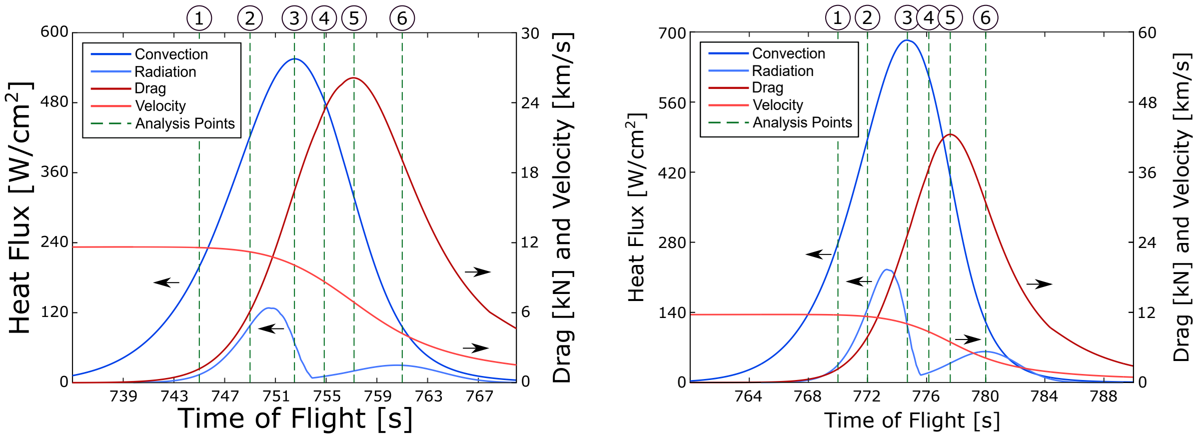

(a) Trajectory 15.9

(b) Trajectory 24.2

Figure 3.1: Results for the semi-empirical correlations for (a) Trajectory 15.9 and (b) Trajectory 24.2.

Table 3.1: Points where the analysis will be performed for Trajectory 15.9.

	Trajectory 15.9					
	Velocity [km/s]	Altitude [km]	Density [g/m^3]	Temperature [K]	Pressure [Pa]	K_n [x10^{-6}]
Point 1	11.58	77.31	0.024	202.03	1.40	3.13
Point 2	11.21	65.43	0.141	230.24	9.31	0.65
Point 3	10.07	55.81	0.486	257.18	35.90	0.26
Point 4	8.63	50.11	0.964	270.65	74.94	0.19
Point 5	6.89	45.62	1.726	266.79	132.16	0.16
Point 6	4.22	40.46	3.599	252.34	260.72	0.20

Table 3.2: Points where the analysis will be performed for Trajectory 24.2.

	Trajectory 24.2					
	Velocity [km/s]	Altitude [km]	Density [g/m^3]	Temperature [K]	Pressure [Pa]	K_n [x10^{-6}]
Point 1	11.56	72.89	0.048	210.86	2.92	1.64
Point 2	11.29	63.71	0.178	235.07	11.99	0.52
Point 3	10.02	52.10	0.758	267.56	58.19	0.18
Point 4	8.73	46.88	1.451	270.32	112.59	0.12
Point 5	6.92	42.25	2.776	257.35	205.07	0.10
Point 6	4.18	37.16	5.888	243.10	410.90	0.12

lation in these simulations. The number is calculated through the use of the following formula:

$$K_n = \frac{k_B T}{(p + \rho \frac{V^2}{2})\sqrt{2}\sigma L} \tag{3.4}$$

where L is the characteristic dimension of the body, in this case, the capsule's radius, σ is the collision effective cross-section and is taken as 10^{-19} m^2, and k_B is the Boltzmann constant.

The region where the continuum Navier–Stokes equations with no slip boundary condition hold is characterized by $K_n \leq 10^{-3}$ [43]. This adimentional number is examined to decide if low-density effects are important and to what extent [23]. Considering that for all selected points, the Knudsen number is well below the 10^{-3} threshold, it is concluded that the use of the Navier-Stokes equations with no slip boundary condition is valid.

Figure 3.2 shows the trajectory points considered for the numerical simulations performed in this work as well as relevant processes taking place along each trajectory. It also depicts the evolution of the Knudsen number along both trajectories.

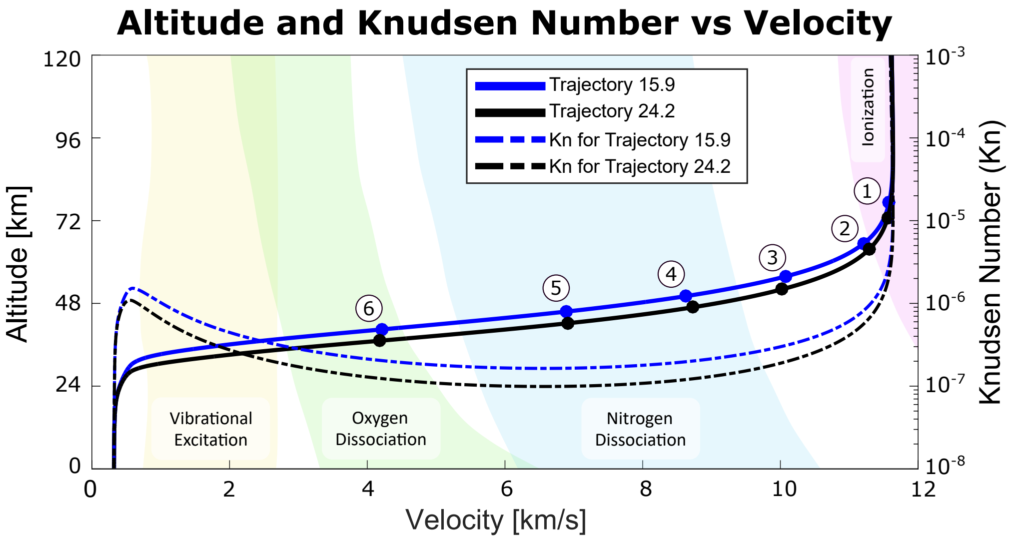

Figure 3.2: Different phenomena present at reentry for both trajectories. Adapted from [23].

3.3 Mesh Generation

The following mesh generation study was performed considering the initial conditions for the peak heating (point 3) of Trajectory 15.9, for which data is presented in table 3.1. In order to perform the described simulations, the use of a suitable mesh is required. Figure 3.3 shows the capsule geometry where the forward body is highlighted in the drawing. The body is axisymmetric and therefore, only half of the front body will be considered in the computational domain. It is assumed that the convective heat fluxes are negligible in the low-density afterbody region (a reasonable assumption shared by the works presented in the state-of-the-art section 1.3).

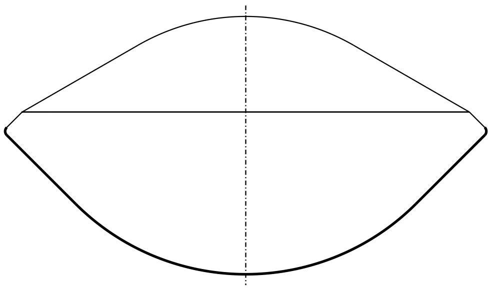

Figure 3.3: DIVER capsule geometry.

Figures 3.4a-d present four mesh configurations that have been considered to discretize the computational domain.

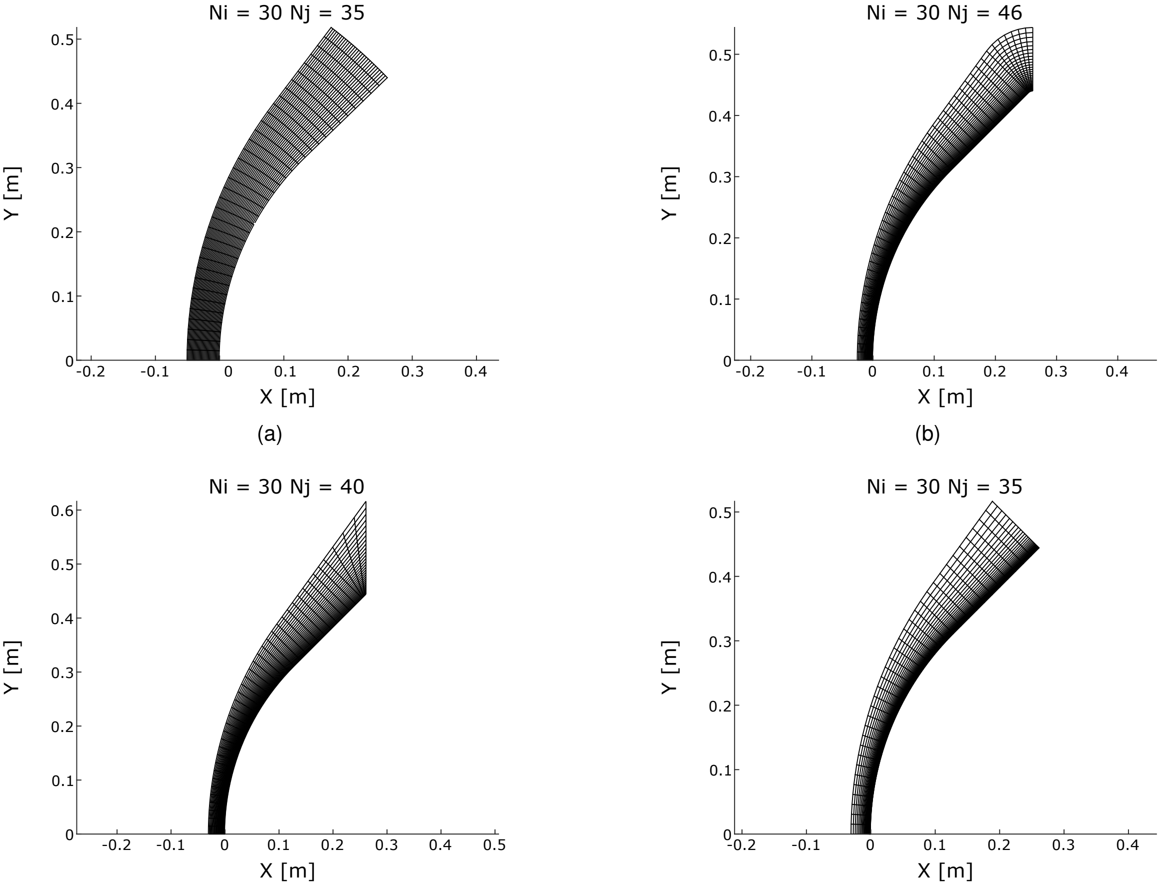

(a)

(b)

(c)

(d)

Figure 3.4: Four different mesh configurations considered during the mesh generation process. Ni stands for the number of mesh cells along the stagnation line. Nj is the number of cells along the capsule surface.

Two main aspects were taken into consideration: 1) mesh refinement at the wall and 2) discretization of the end corner of the capsule. As we want to study the wall convective heat fluxes, the boundary layer has to be fully captured by the mesh and, therefore, the refinement of the mesh near the capsule surface is required. Refining the mesh in the shock wave region was not done, since the full capture of this region is only relevant when determining the radiative heat fluxes. Mesh (a) does not have this refinement and hence was discarded. Regarding the discretization of the capsule's end corner, meshes (b) and (c) both account for it. Mesh (c) produced the best results out of the two ((b) and (c)). Nevertheless, mesh (d) presented the best overall results and even though not considering the capsule corner, the results were similar to those obtained with mesh (c) (with corner). Based on the aforementioned discussion, the final mesh adopted was that shown in Fig.3.4d.

3.3.1 Convergence Study

After selecting the best mesh configuration, a fine-tuning of the number of mesh cells was performed, to obtain the best results at the least computational effort. Figure 3.5 shows a comparative analysis of (a) the temperature profiles along the stagnation line and (b) the wall heat fluxes for three mesh resolutions. Ni refers to the number of mesh cells along the stagnation line.

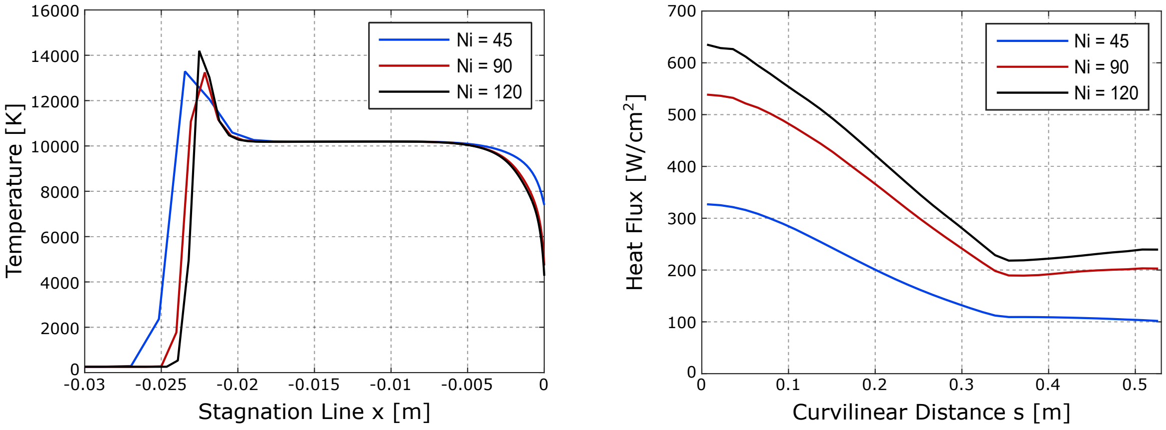

(a) Stagnation Line Temperature (b) Wall Heat Flux

Figure 3.5: Stagnation Line Temperature (a) and Wall Heat Flux (b) profiles for three different values of Ni, where Ni is the number of mesh cells along the stagnation line.

Analysing Fig.3.5a it can be seen that for Ni = 120 (black line) the peak of the gas temperature is 4% higher than for Ni = 45 (blue line) and Ni = 90 (red line). Moreover, for Ni = 45 the gas temperature decreases 73% less than for Ni = 90 and 120. Due to these discrepancies it is concluded that the mesh with Ni = 45 is too rough to be used in the desired simulations.

Figure 3.5b shows the wall heat flux profiles for the same Ni values, along the capsule wall referential (curvilinear distance s). The mesh with Ni = 120 is the one predicting a higher value of the wall heat fluxes, with a peak of about 640 W/cm^2. For Ni = 90 and Ni = 45, this value is 16% and 56% lower, respectively. The difference in peak levels agrees well with the previous analysis of the gas temperature profiles at the stagnation line.

Due to the fact that the results obtained for Ni = 90 and Ni = 120 are significantly closer than those obtained for Ni =45, it is concluded that the mesh with Ni = 120 is the most suitable for these simulations. Meshes with higher refinements were tested, however these were very computationally expensive and the very small grid size near the boundary layer prevented a meaningful convergence.

Figure 3.6 shows the final mesh after the convergence study, with Ni = 120. This mesh is the one which will accurately capture the peak values of the wall heat flux.

3.4 Boundary Conditions

Figure 3.7 shows the boundary conditions considered in the simulations performed in this work. The isothermal boundary condition at the wall is set to T = 1200 K.

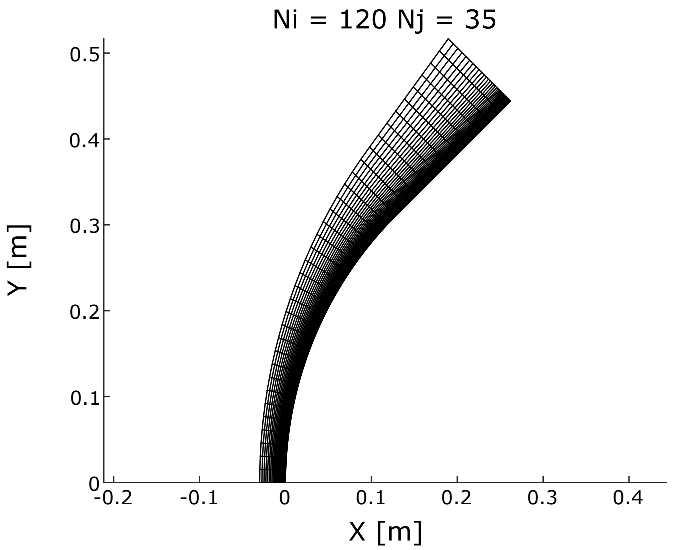

Figure 3.6: Selected final mesh configuration. Ni stands for the number of mesh cells along the stagnation line. Nj is the number of cells along the capsule surface.

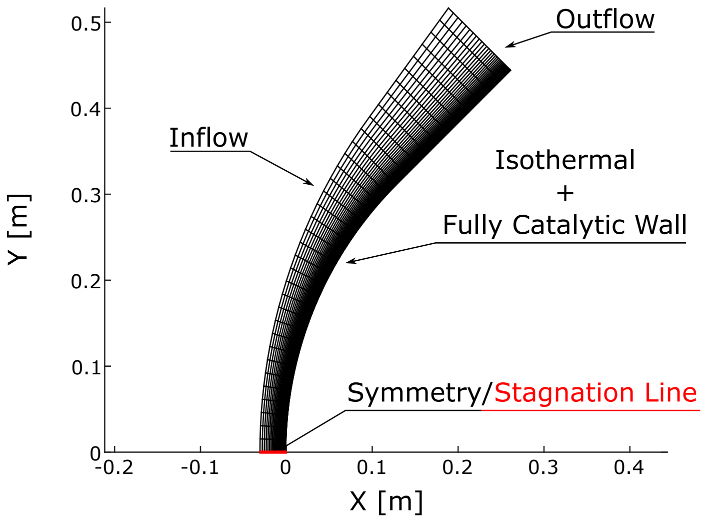

Figure 3.7: Boundary conditions considered for the CFD domain.

3.4.1 Catalycity

In addition to the boundary conditions previously stated, a condition will be considered to account for how the flow interacts with the surface. This interaction is characterized by exothermic reactions that can also consume the surface material, which introduces complexity in the design process. The boundary condition can either be noncatalytic, in which it is assumed that the wall is not affected by the flow and hence there is no recombination of the atoms that collide with the surface, or catalytic, where the flow particles recombine to some extent at the capsule surface. The present work considers a fully catalytic boundary condition, which refers to the assumption that all atoms which collide with the surface recombine. It represents the upper boundary of the overall heat flux (i.e. the worst case scenario) since there is the extra heat flux originating from the exothermic recombinations. Figure 3.8 shows a graphical representation of the assumptions made by (a) noncatalytic and (b) catalytic boundary conditions.

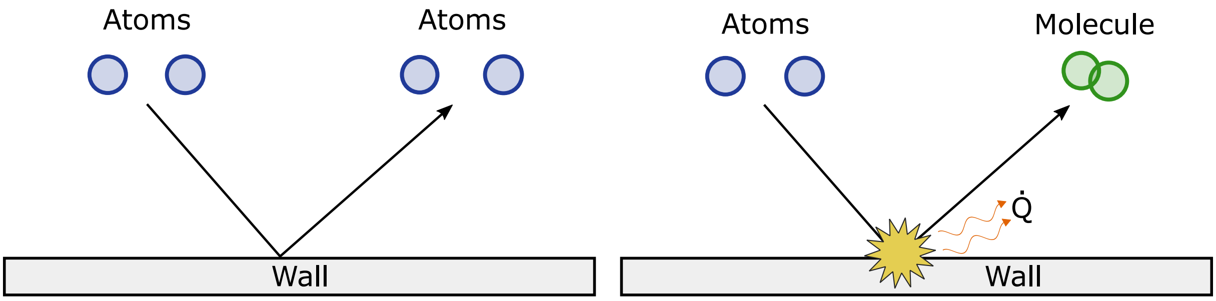

(a) Noncatalytic Wall (b) Catalytic Wall

Figure 3.8: Existence of recombination depends on the considered wall boundary condition.

3.5 Simulation Inputs

To be able to run the simulations proposed in code SPARK, a input file must be filled with the following parameters:

- `Simulation` - Sets the type of simulation to be performed. In the present work, a 2D axisymmetric geometry is considered.
  - `Simulation_Type` = 2D_Axi
- `Flow` - Sets the flow type to be considered in the simulation. In this case, the gas is set to nonequilibrium conditions. Moreover, the set of equations to be solved are the Navier Stokes equations for a reacting flow.
  - `Gas_Model` = Nonequ_Gas
  - `Flow_Type` = Navier_Stokes
- `Solver` - Sets the method to solve the previously established set of equations.
  - `Time_Discretization` = Explicit or Implicit
  - `Cfl` - depends on the type of simulation being considered
- `Gas_State` - Sets the gas mixture initial conditions. Depends on the trajectory point being considered.
  - `Density`
  - `Temperature`
  - `Velocity`
  - `Mole_Fractions` = N2:0.79 O2:0.21 for all simulations
- `Kinetic` - Sets the kinetic parameters for the simulations, in particular the kinetic scheme. The present work considers, as previously stated, the 11 species air kinetic scheme by Park [25].
  - `Kinetic_Scheme` = Air11-Park2001

- `Multi_Temperature` - Sets the parameters required in case the multi-temperature model is being considered. The present work considers Park's two-temperature model.
  - `Electronic_nonequ_model` = Translational_Excitation_Vibration
- `Transport` - Sets the parameters regarding the transport model being considered.
  - `Transport_Model` = Wilke or Gupta

3.6 Simulation Strategy

Hypersonic flows, alongside turbulent flows, represent some of the most challenging and unforgiving problems in contemporary CFD applications. Furthermore, compared to orbital reentry velocities around 7 km/s, superorbital entry simulations around 11 km/s are even more challenging due to convergence issues. In this section, the strategy used to cope with these issues is discussed. It encompasses three different approaches where models are switched to improve computation speed and convergence:

Euler vs. Navier-Stokes: Simulations are firstly initiated for the Point 3 of Trajectory 15.9, considering the reactive Euler equations to begin with, neglecting transport terms. Once the shock wave position stabilizes, the Navier-Stokes equations are applied in order to take into account the boundary layer near the surface of the capsule. All simulations, apart from the one specific to the analysis of thermal nonequilibrium, considered thermal equilibrium. This is due to the fact that in the boundary layer there is thermal equilibrium and this is the relevant region for the analysis of the convective heat flux.

Wilke vs. Gupta-Yos: Secondly, all the simulations consider the Wilke transport model to begin with. All the simulations considering the Gupta-Yos model were performed with the simulation with the Wilke model as the baseline.

Initialization of further trajectory points from the converged solution for point 3 of Trajectory 15.9: Thirdly, to further minimize the convergence time, point 3 of Trajectory 15.9 was used as a baseline for all the other points in both trajectories. This minimizes time since only slight changes are expected in the flowfield, namely shock detachment. It is expected that the residual rise at the beginning simply due to the change in the initial conditions. However, when compared to the time associated to a simulation from the beginning to convergence (where the shock wave initiates at the wall and migrates towards its equilibrium position), the time required for convergence in a simulation starting with point 3 is significantly smaller.

Implicit vs. Explicit: Finally, the best way to minimize convergence time is to consider an implicit time discretization. This method is not always used because of the computational effort requirements and because the simulation often crashes if the shockwave is not yet close enough to its stabilized position. To perform the simulations in all the points of the trajectory at the same time, very few iterations (1000) had to be considered each time, due to the computer memory requirements. Using the explicit time discretization, many iterations were performed each time (usually 100000) however, the maximum CFL possible was very low in order to prevent the simulation from crashing, resulting in a very high convergence time for each solution (up to 1 month, depending on the mesh and solution parameters considered). Using an implicit time discretization, the CFL can be raised from small values to values as high as 100 and thus the convergence time is very low.

When performing these simulations, the CFL and the number of iterations has to be constantly monitored and changed to prevent the simulation from crashing and obtaining adequate results with the minimum convergence time. Figure 3.9 shows the effects of these strategies in the residual profile of the simulation at Point 5 in Trajectory 15.9, beginning at the starting point for Point 3 simulation.

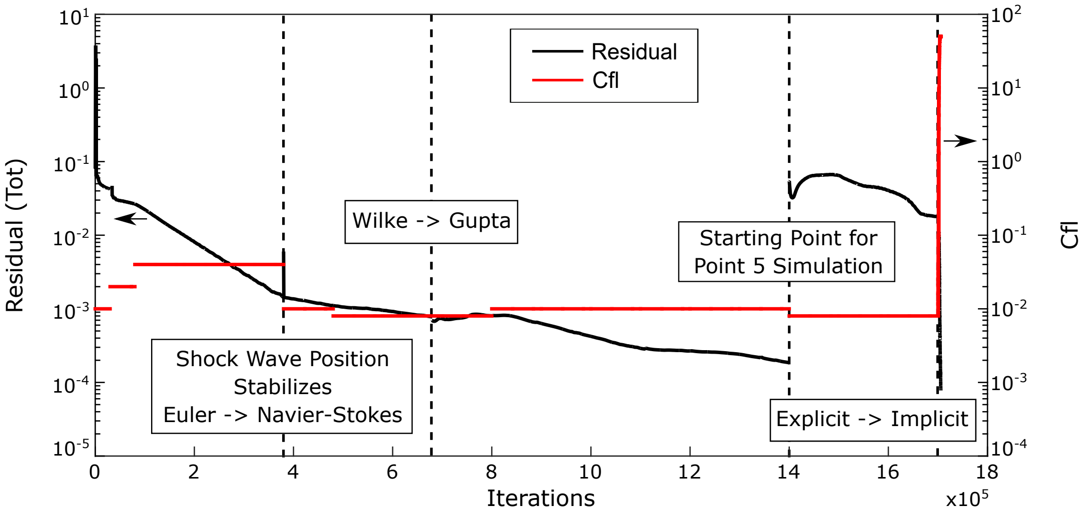

Figure 3.9: Residual profile and CFL values along the simulation performed at point 5 in Trajectory 15.9, beginning at the starting point for Point 3 simulation.

Figure 3.9 shows that the residual rises slightly when changing from Euler to Navier-Stokes solver. This is to be expected since the viscosity was not previously considered. Afterwards, at the transition from Wilke to Gupta-Yos transport model, the residual stabilizes for a few iterations before continuing its decrease. Once the simulation at point 5 begins, the residual rises steeply, however the starting point is lower than the point for the whole simulation at iteration 0, which results in a lower convergence time. Finally, there is a steep rise in CFL and a steep decrease in residual when the implicit time discretization method is used. The residual decreases from 10^{-2} to 10^{-4} in simply 6000 iterations.

Chapter 4

Results and Discussion

CFD simulations are analysed and discussed in this chapter. The impact of the transport model and reentry velocity is ascertained in section 4.1. The impact of applying a multi-temperature model as opposed to considering thermal equilibrium is discussed in section 4.2. A detailed analysis of the results obtained for the trajectory point corresponding to the peak in convective heating is shown in section 4.3. Finally, section 4.4 presents the heat flux results obtained for all trajectory points.

4.1 Impact of Transport Model and Velocity

The following analysis was performed for point 3 of Trajectory 15.9, considering thermal equilibrium. The results considering the two different transport models were compared. The impact of the freestream velocity was studied by comparing the results obtained in the present work against those obtained by Loureiro [44]. Both simulations were performed using code SPARK and considered the same kinetic scheme and thermal equilibrium. In the simulations ran by Loureiro [44] the RAM-C II capsule geometry and a reentry velocity of 7.65 km/s were considered.

Figure 4.1 shows the stagnation line temperature profile for both mixing rules, for the reentry speed of 10 km/s (a) and 7.65 km/s (b).

Focusing on the results obtained in the present work (Fig. 4.1a), the greatest discrepancy for each transport model lies in the boundary layer. Around x = -0.0025 m, the Gupta-Yos model (black line) shows a steeper decrease in temperature when compared to the Wilke model (red line). Moreover, the decline in temperature takes place a bit earlier, at around x = -0.005 m. Looking at the peak region, there is a slight difference in the peak temperature value for each model. The Gupta-Yos model predicts a peak temperature of 7% higher than the Wilke model.

Comparing the results obtained for each reentry velocity (Fig. 4.1), there are two main differences. 1) The results agree better at lower velocities, which will be addressed later on at the end of this section, and 2) that for the lowest velocity, there is no region where the temperature stabilizes. The reason for the absence of this region is that the chemical reactions, in the shock region, occur at a slower rate, when compared to the highest velocity. In the 10 km/s case, chemical reactions occur much faster and

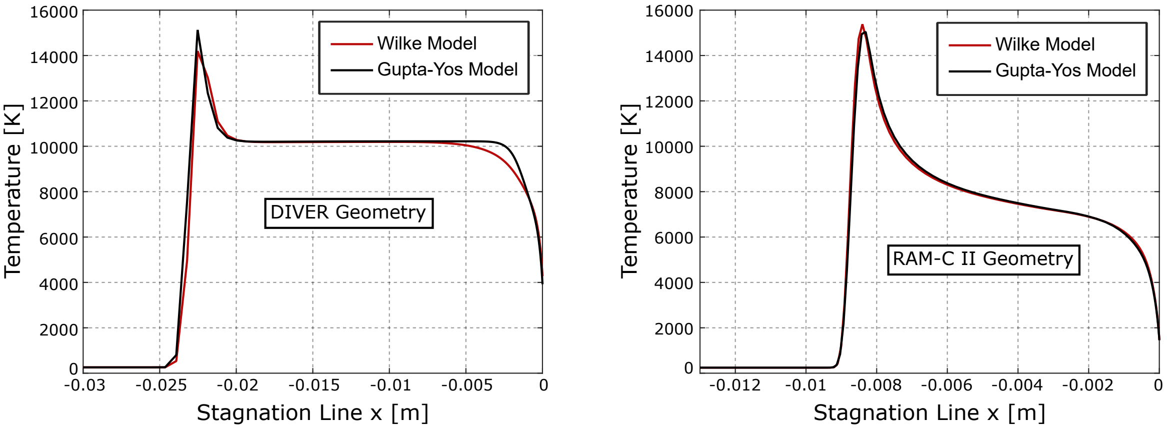

(a) 10 km/s (b) 7.65 km/s

Figure 4.1: Stagnation line temperature profiles for both mixing rules, for a reentry speed of 10 km/s (a) and 7.65 km/s (b).

chemical equilibrium may be reached before the flow reaches the boundary layer region. This explains why the temperature remains constant. Once in chemical equilibrium, exothermic and endothermic reactions balance themselves.

Figure 4.2 shows the mass source terms for atomic oxygen at (a) 10 km/s and (b) 7.65 km/s. At the shock, the reactions resulting in the creation of atomic oxygen are occurring at a higher rate (30% higher) for the highest velocity case.

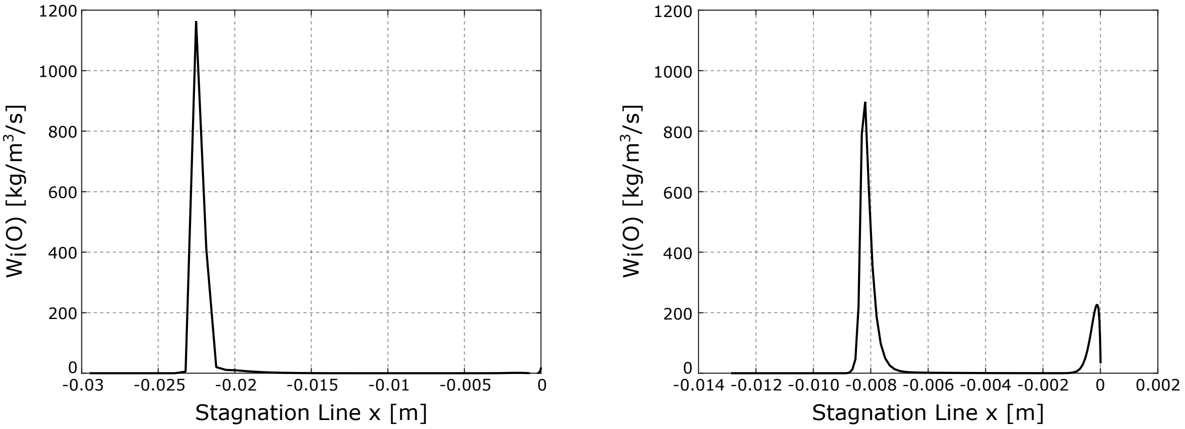

(a) 10 km/s (b) 7.65 km/s

Figure 4.2: Oxygen mass source terms for a reentry speed of 10 km/s (a) and 7.65 km/s (b).

Comparing the peak temperature for both reentry velocities, these appear similar. However, one would expect the value corresponding to the highest velocity to be much higher (since the resulting shock would present a higher temperature gradient). Due to the roughness in this area, of the mesh considered in the present work, the shock peak is not fully captured and therefore, the peak temperature seems similar in both cases. Appendix A presents simulation results for the RAM-C II capsule geometry and mesh considered in Loureiro [44] with the reentry conditions of the present work. The results obtained present a higher temperature peak, when compared to the results obtained by Loureiro [44] and thus prove that the similarity between the peak temperatures obtained for each reentry velocity is attributed to the roughness of the considered mesh. Although the peak temperatures appear to be the same, a distinct difference between the results for each reentry velocity (Fig. 4.1) is the temperature gradient at the capsule surface, which is much steeper for the highest velocity. Consequently, a higher heat flux at the stagnation point is expected for the highest reentry velocity.

Figure 4.3 shows the wall heat flux profiles for both transport models, for a reentry speed of 10 km/s(a) and 7.65 km/s(b).

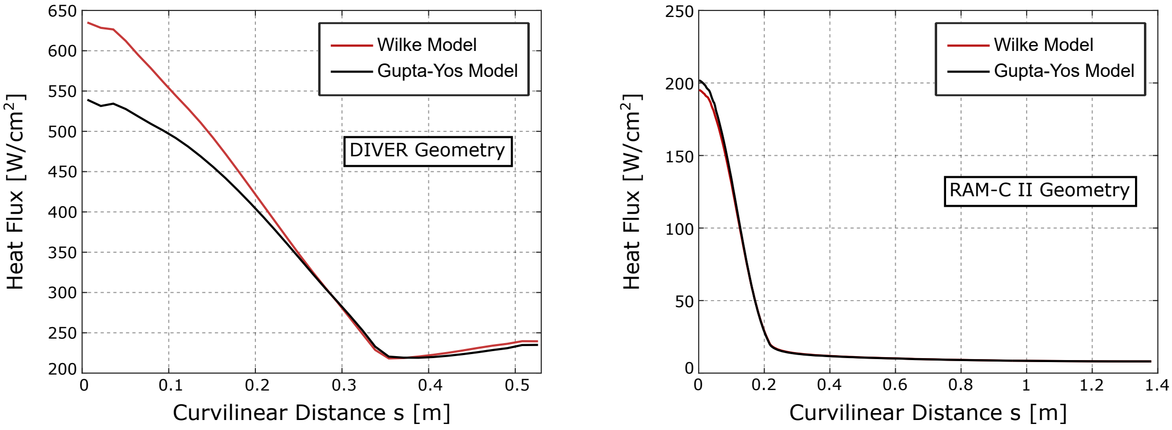

(a) 10 km/s

(b) 7.65 km/s

Figure 4.3: Wall Heat Flux profiles for both mixing rules, for a reentry speed of 10 km/s (a) and 7.65 km/s (b).

Focusing on the results for the 10 km/s case (Fig. 4.3a), there is a great difference in the wall heat flux profiles depending on the selected transport model. Both curves show the same overall tendency, sinking from s = 0 m up to s $\approx$ 0.35 m and subsequently rising gently until s $\approx$ 0.52 m. However, the peak heat flux obtained is 640 W/cm^2 for the Wilke model, 19% higher than for the Gupta-Yos model. For both curves, there is a slight disturbance around s = 0.04 m, which is currently attributed to numerical issues. A possible cause for this may be the carbuncle problem [45]. It is defined as a local displacement of the bow shock wave shape near the stagnation line, which compromises the accuracy of the heat transfer predictions made by numerical simulations of hypersonic flows. It is most prominent in CFD simulations within the blunt nose region of an aerodynamic vehicle on axisymmetric grids [45]. Although some efforts have been done to improve simulation accuracy, none have yet succeeded in removing the problem.

Analysing the results obtained for a reentry velocity of 7.65 km/s (Fig. 4.3b), a good agreement between both models is found, except for a minor distinction near s = 0 m. The peak value for the Wilke model is $\approx$ 190 W/cm^2, 5% lower than that for the Gupta-Yos model.

Comparing the results obtained for both reentry velocities, the heat fluxes at the wall are about three times higher for 10 km/s, which agrees well with the increased temperature gradient at the surface.

The results obtained for both transport models agree better at the lowest velocity (as shown in Figs. 4.1 and 4.3). This is related to the increase in the degree of ionization of the flow at higher velocities, since these models were formulated assuming a weakly ionized gas. Figure 4.4 shows a comparative analysis of the electron molar fractions for both transport models and both velocities. The electron molar fraction is overall about two orders of magnitude higher for the reentry velocity of 10 km/s. Consequently, the results do not agree, as well as for lower reentry velocities, because the flow is more ionized.

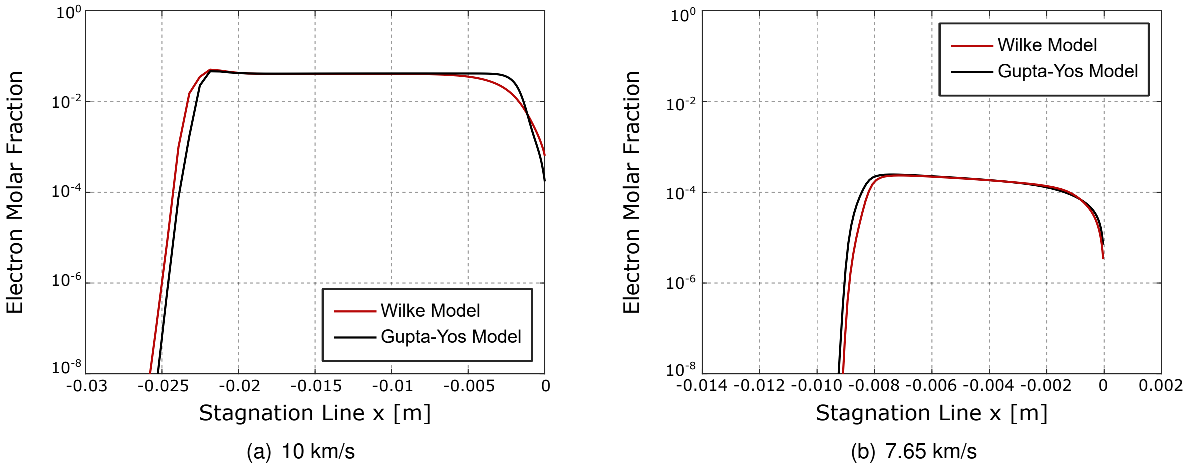

(a) 10 km/s

(b) 7.65 km/s

Figure 4.4: Electron mole fraction profiles for both mixing rules, for a reentry speed of 10 km/s (a) and 7.65 km/s (b).

The Gupta-Yos model is assumed to provide the most accurate results owing to the fact that the true nature of the viscosity collisions is taken into account. Consequently, the following simulations will consider this model for the transport properties.

4.2 Impact of Multi-Temperature Model

As seen in section 2.4, Park's two-temperature model is implemented in SPARK to account for thermal nonequilibrium. Figure 4.5 shows profiles for (a) the stagnation line temperatures and (b) the wall heat flux for thermal nonequilibrium and thermal equilibrium. This simulation was also performed on point 3 of trajectory 15.9. A fully catalytic boundary condition at the surface and the Gupta-Yos transport model were considered.

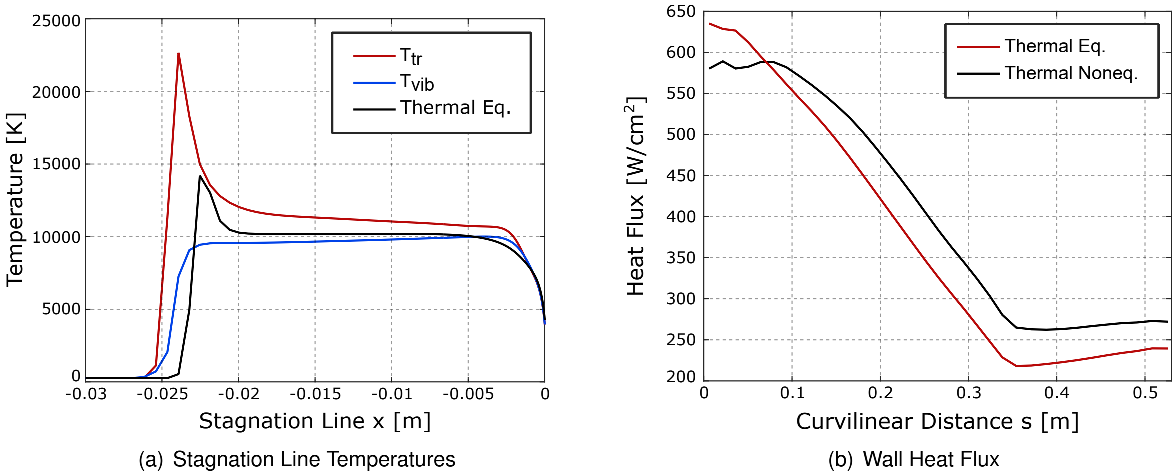

(a) Stagnation Line Temperatures

(b) Wall Heat Flux

Figure 4.5: Profiles for (a) the stagnation line temperatures (b) wall heat flux for thermal equilibrium and nonequilibrium.

Focusing on Fig.4.5a, the translational/rotational temperature (red line) profile follows the same overall trend as the temperature profile considering thermal equilibrium (black line), it rises steeply in the shock region (x = -0.022 m) and afterwards, although it does not stabilize, it slowly decreases up to x = -0.005. However, the peak in translational temperature reaches 22000 K, 27% higher than for the thermal equilibrium case. The vibrational/electron/electronic excitation temperature (blue line) follows a more distinct profile, firstly it increases suddenly at x = -0.025 m reaching just under 10000 K. Afterwards it gradually increases until 10000 K at x = -0.005 m. The discrepancy in the profiles for the translational/rotational temperature and the vibrational/electron/electronic excitation temperature leads to the conclusion that there is a very strong thermal nonequilibrium, as would be expected for the flow initial conditions. Thermal equilibrium is just reached at the boundary layer.

Figure 4.5b presents the wall heat flux results obtained for thermal equilibrium (red line) and thermal nonequilibrium (black line). It is shown that both present the same overall trend after s = 0.09 m. Before this point, both heat fluxes present a disturbance at s = 0.04 m, supporting the previous assumption of the carbuncle problem. The stagnation point heat flux predicted for the thermal nonequilibrium is approximately 580 W/cm^2, 9% lower than the one predicted for the thermal equilibrium case. It would be expected that the heat fluxes at the wall be the same along the capsule since thermal equilibrium is reached at the boundary layer. However, the temperature gradients differ, leading to slightly different heat fluxes. Nonetheless, the differences remain lower than 10% in the critical region of the stagnation streamline, allowing for the use of a more simplified and time-efficient single-temperature thermochemical model in the rest of the analysis.

4.3 Peak Heating Point Analysis

In this section, the results obtained using the input data for point 3 of Trajectory 15.9 are presented considering the Gupta-Yos transport model, thermal equilibrium and a fully catalytic wall. This is a key point in the trajectory for the design of the TPS, since it corresponds to peak convective heating.

Figure 4.6 shows the results for (a) species mole fractions and (b) temperature, pressure and velocity profiles along the stagnation line.

Figure 4.6a shows that the mole fractions of N_2 and O_2 decrease after the bow shock (x = -0.022 m), whereas the rest of the species mole fractions increase after this point. Gas chemical composition stabilizes from x = -0.020 m up to x = -0.003 m. Afterwards, concentrations of N_2, O_2 and NO increase due to the recombination reactions taking place at the capsule surface. This is balanced by the decrease in the molar fractions of species N_2^+, O_2^+, NO^+, e^- and N. One would expect the molar fraction of O to decrease at the surface due to the recombination of O_2 ($O + O + \text{wall} \Rightarrow O_2$), however that is not the case, owing to the fact that this species is involved in more recombination reactions. O^+ decreases in molar fraction, suggesting it is recombining with e^- and forming O. This latter reaction is taking place at a higher rate than the recombination of O_2 resulting in a decrease in atomic oxygen molar fraction near the surface. N^+ concentration also decreases, suggesting recombination of N^+ and e^- as well. However, this reaction is taking place at a slower rate when compared to the recombination of N and N,

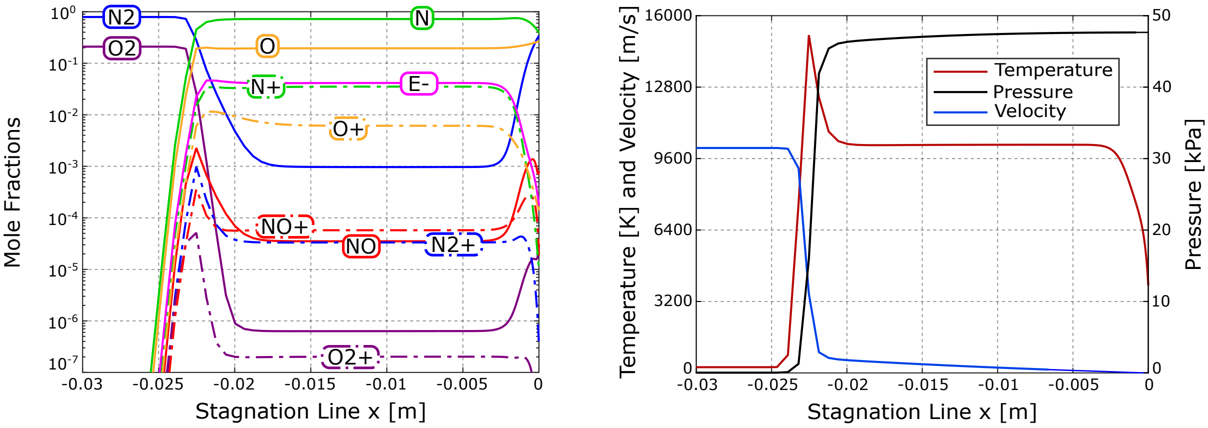

(a) Species Mole Fractions

(b) Temperature, Pressure, Velocity

Figure 4.6: Stagnation line profiles for (a) species mole fractions and (b) temperature, pressure and velocity.

leading to a decrease in the atomic nitrogen molar fraction.

Focusing on Fig. 4.6b, for the shock peak (x = -0.022 m) there is an increase in temperature and pressure, whereas the velocity decreases. After reaching its peak, temperature decreases rapidly until it stabilizes at 10000 K, from x = -0.02 m up to x = -0.003 m. It then decreases abruptly until reaching the capsule surface at x = 0 m with the imposed wall temperature. Regarding the pressure, it rises until 47.7 kPa in the shock region, at x = -0.022 m, and remains stable until the capsule wall (x = 0 m). The velocity drops abruptly from 10000 to $\approx$ 960 m/s in the shock region and afterwards gradually decreases until V = 0 m/s at the capsule wall.

Figure 4.7 depicts the 2D fields for (a) temperature, (b) atomic nitrogen mole fraction, (c) electron number density and (d) oxygen mole fraction.

Figure 4.7a shows the shock wave position very clearly due to the abrupt temperature rise. Towards the outflow boundary condition the temperatures in the shock layer are gradually lower (above Y = 0.3 m). This is due to the shock wave position relative to the flow direction. In the stagnation line, the shock wave is normal to the flow direction and the temperature gradient is very high. Moving along the shock wave, it becomes an oblique shock resulting in a lower temperature gradient.

Figure 4.7b shows that ahead of the shock, there are no nitrogen atoms, since there is only N_2 and O_2 making up the atmosphere composition. In the shock region, the N mole fraction starts increasing and continues to do so up to the boundary layer. Near the capsule surface, the N mole fraction decreases again, due to the recombination reactions taking place using the surface as a catalyst. The increase in atomic nitrogen concentration in the shock region is gradually less steep moving towards the outflow boundary (above Y = 0.3 m). This agrees well with the decrease in temperature in this region, as explained before.

Figure 4.7c presents the electron number density along the flow. The electrons' concentration is higher in the shock layer region closest to the stagnation line (up to Y = 0.3 m). Due to the high temperatures, ionization reactions occur and consequently ions and electrons are formed. Above Y = 0.3 m, in the region where the temperature is lower, there are fewer reactions of this type and thus,

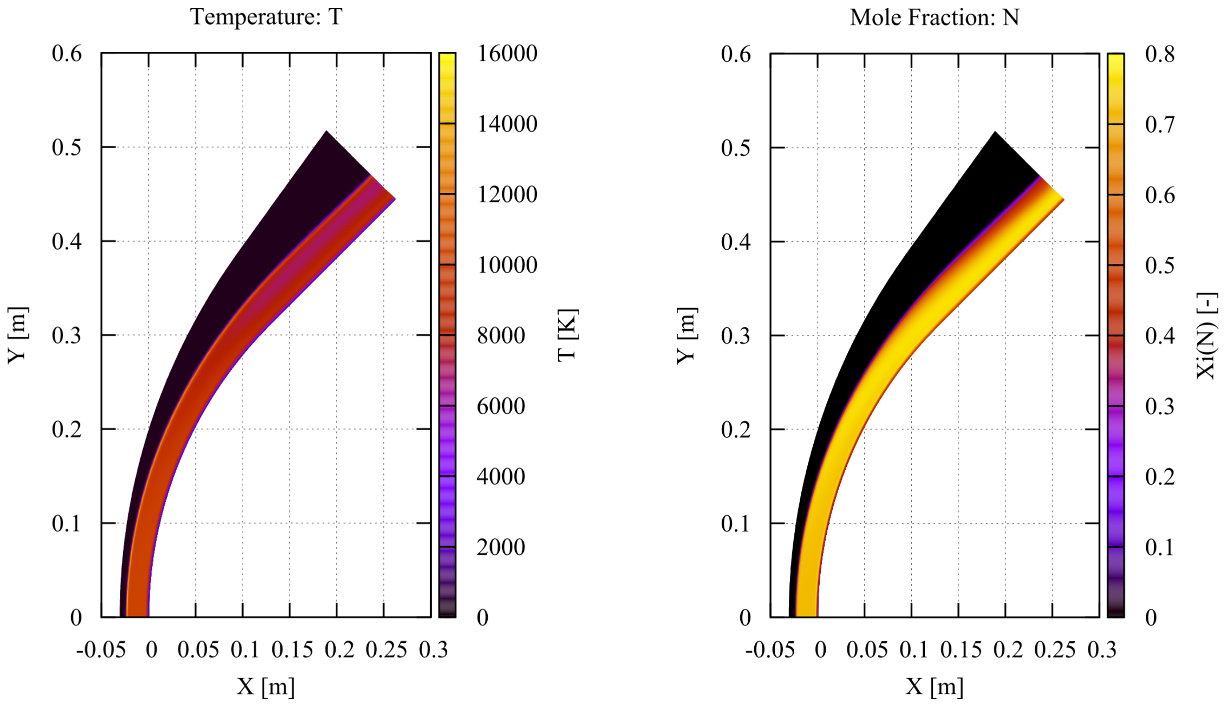

(a) Temperature (b) Atomic Nitrogen Mole Fraction

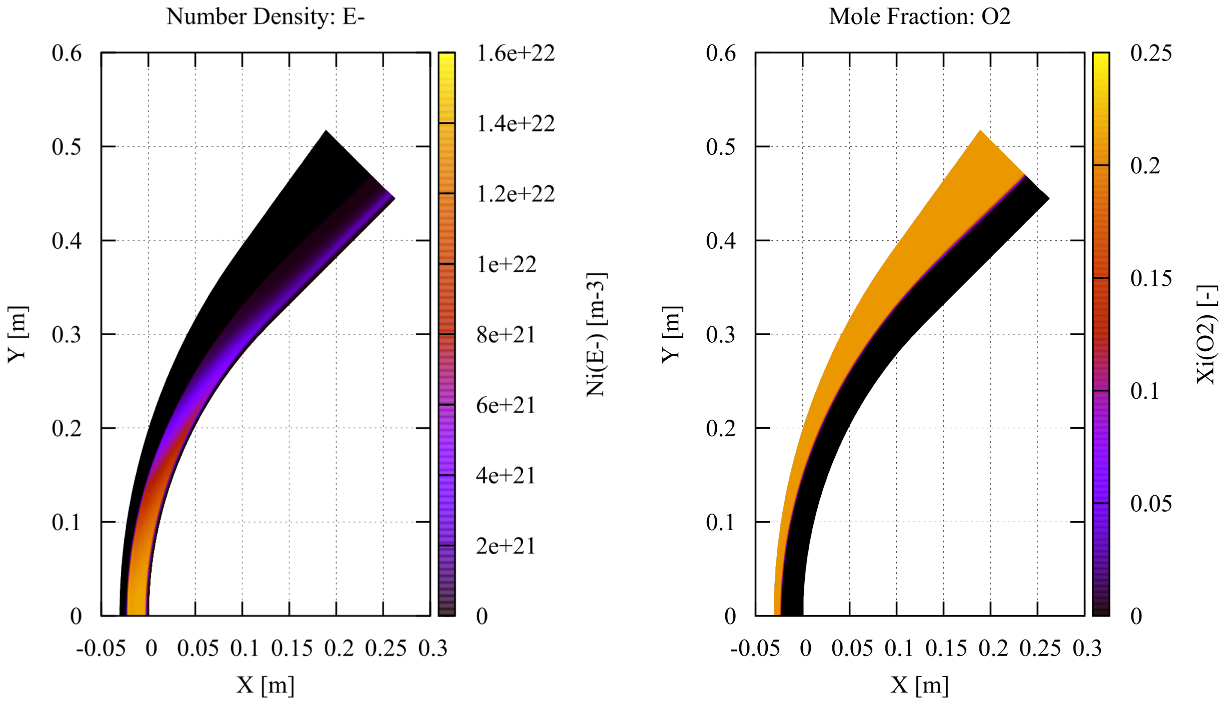

(c) Electron Number Density (d) Oxygen Mole Fraction

Figure 4.7: Flow field results for (a) temperature (b) atomic nitrogen mole fraction (c) electron number density and (d) oxygen mole fraction.

the electron number density decreases. Close to the surface, the electron number density decreases abruptly due to the recombination reactions taking place.

Figure 4.7d shows the molar fraction of oxygen along the flow. Before the shock, the oxygen molar fraction is 0.25. In the shock layer, dissociation reactions occur and the concentration of this species decreases sharply. All oxygen was dissociated and concentrations are very low. Above Y = 0.3 m, in the region where the temperature is lower, it is shown that the decrease in concentration is less abrupt when compared to the region closest to the stagnation line.

4.4 Heat Fluxes for Project DIVER

For the key trajectory points detailed in section 3.2, CFD simulations were performed considering the Gupta-Yos transport model, thermal equilibrium and a fully catalytic wall.

Figure 4.8 compares the data obtained in this work with the Sutton-Graves correlation for the convective heat flux along (a) Trajectory 15.9 and (b) Trajectory 24.2.

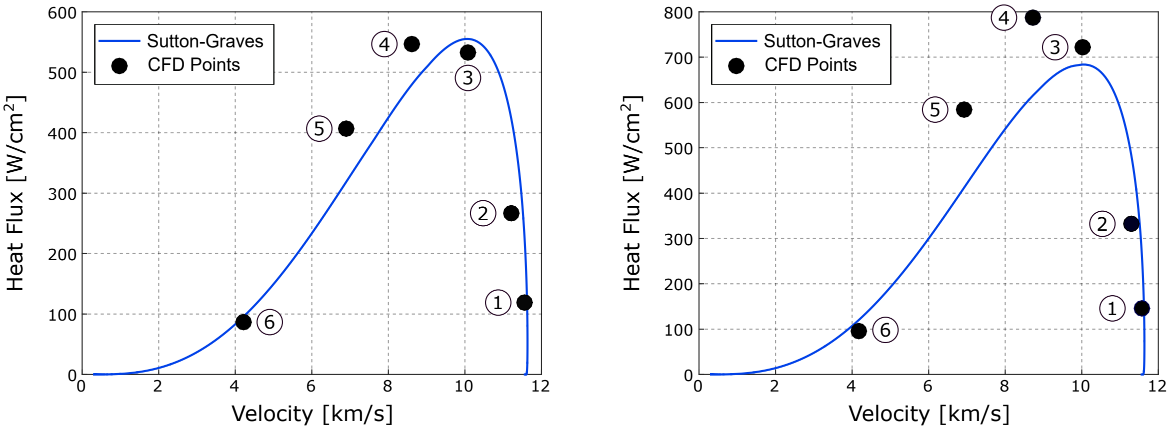

(a) Trajectory 15.9

(b) Trajectory 24.2

Figure 4.8: Comparison of the data obtained in this work and the Sutton-Graves correlation for the convective heat flux along (a) Trajectory 15.9 and (b) Trajectory 24.2.

For both trajectories, some CFD points predict a higher convective stagnation heat flux than the Sutton-Graves equation. The highest discrepancy (48%) was found for Trajectory 24.2 in the point with the highest velocity, point 1. The peak heating point, for both trajectories is point 4, as opposed to number 3 in the correlation. The discrepancies found between the results stem from the fact that, as mentioned in section 3.2, the Sutton-Graves equation assumes chemical equilibrium. Overall, the Sutton-Graves correlation is shown to be quite satisfactory from the perspective of capsule design.

Chapter 5

Conclusions

5.1 Achievements

A successful comparison between the Wilke and the Gupta-Yos transport models was performed for an hyperbolic Earth reentry. The Gupta-Yos model is assumed to yield better results, on account that it considers the true nature of particle collisions. Moreover, it was found that for higher reentry velocities, the selection of the method to calculate transport properties influences the results more than for lower velocities, on account of the increased degree of ionization of the flow.

An analysis of the impact of applying a multi-temperature model was performed for reentry conditions at 10 km/s. Park's two-temperature model was considered. At the shock, the translational/rotational temperature reached a temperature value 144% higher than the vibrational/electron/electronic excitation temperature. The flow presents a very strong thermal nonequilibrium, as would be expected. This does not impact the overall aerothermodynamics of the flow due to the fact that the concentrations of the molecules in the shock layer are very low (0.1% for N_2, 0.0001% for O_2 and 0.01% for NO) and thus constitute a very small percentage of the flow composition. In this region, the ions and atoms characterize the flow and hence the vibrational temperature loses its meaning.

The trajectory point corresponding to peak convective heating was fully analysed. The species molar fractions validated the assumption of a fully catalytic wall boundary condition. The analysis for this point allowed for a better understanding of the physical processes occurring at superorbital reentry conditions.

The stagnation point convective heat flux was analysed for all the key trajectory points and compared to the Sutton-Graves correlation. The results agreed reasonably with the correlation, presenting a relative discrepancy of up to 48%. This was attributed to the fact that the correlation assumes that the flow is in chemical equilibrium. The use of the semi-empirical correlations, as considered in the present work, does not revoke the need for CFD simulations for further fine-tuning as pertaining to the sizing of spacecraft TPS.

5.2 Future Work

The next step in this work would be the assessment of the radiative heat fluxes at the surface of the capsule. Simulations for the six points of both trajectories considering the two-temperature model would be performed and the results would serve as input for a radiation code (since radiation depends on the population of the excited states and convection of the fundamental states). This analysis would result in a more accurate assessment of the total heat flux at the surface and a better understanding of the flow behaviour in these conditions. A further comparison against the Tauber and Sutton correlation could be performed to assess its accuracy at superorbital reentry conditions.

Knowing the total heat flux at the capsule surface, a suitable TPS can be designed, as the result of this work, in the scope of project DIVER. Selection of the materials and corresponding thickness is also a possible next step for the present work.

A comparison against Newton methods could also be performed. This would further validate the use of the models applied in these simulations and the implementation performed in SPARK.

Even though this work was not on time for this thesis manuscript, it is currently under way.

Bibliography

[1] W. J. O'Neil and C. Cazaux. The Mars Sample Return Project. *Acta Astronautica*, 47:453–465, 2000.

[2] M. Lino Da Silva. *Simulation des propriétés radiatives du plasma entourant un véhicule traversant une atmosphère planétaire à vitesse hypersonique - Application à la planète Mars*. PhD thesis, Université D'Orléans, 2004.

[3] U. Derz and W. Seboldt. Mars sample return mission architectures utilizing low thrust propulsion. *Acta Astronautica*, 77:83–96, 2012.

[4] A. Pickering. CDF Study Report - Phobos Sample Return - Phobos Moon of Mars Sample Return Mission. Technical report, ESA, 2014.

[5] J. J. Bertin. *Hypersonic Aerothermodynamics*. AIAA, 1994.

[6] M. D. Clemente and D. Ferrarella. Convective and Radiative Heat Flux Estimation on a Re- Entry Capsule. In *10th AIAA/ASME Joint Thermophysics and Heat Transfer Conference*, 2010.

[7] P. A. Gnoffo. Planetary-entry Gas Dynamics. *Annual Review of Fluid Mechanics*, 31:459–494, 1999.

[8] C. Park. Stagnation-Region Heating Environment of the Galileo Probe. *Journal of Thermophysics and Heat Transfer*, 23:417–424, 2009.

[9] J. S. Shang and S. T. Surzhikov. Simulating Stardust Earth Reentry with Radiation Heat Transfer. *Journal of Spacecraft and Rockets*, 48:385–396, 2011.

[10] V. L. Kovalev and A. F. Kolesnikov. Experimental and Theoretical Simulation of Heterogeneous Catalysis in Aerothermochemistry (a Review). *Fluid Dynamics*, 40:669–693, 2005.

[11] K. J. Higdon, D. B. Goldstein, and P. L. Varghese. Sensitivity Analysis of Direct Simulation Monte Carlo Parameters for Ionizing Hypersonic Flows. *Journal of Thermophysics and Heat Transfer*, pages 1–13, 2017.

[12] M. Lino Da Silva, B. Brotas de Carvalho, A. Smith, and L. Marraffa. High-Pressure H2/He/O2 Combustion Experiments for the Design of the ESTHER Shock-Tube Driver. In *46th AIAA Thermophysics Conference*, 2016.

[13] R. K. Hanson and D. Baganoff. Shock-Tube Study of Nitrogen Dissociation Rates Using Pressure Measurements. *AIAA*, 10:211–215, 1972.

[14] C. Park. Two-Temperature Interpretation of Dissociation Rate Data for N2 and O2. In *AIAA 26th Aerospace Sciences Meeting*, 1988.

[15] K. A. Trumble, I. Cozmuta, S. Sepka, P. Jenniskens, and M. Winter. Postflight Aerothermal Analysis of the Stardust Sample Return Capsule. *Journal of Spacecraft and Rockets*, 47:765–774, 2010.

[16] R. A. Mitcheltree, R. G. Wilmoth, F. M. Cheatwood, G. J. Brauckmann, and F. A. Greene. Aerodynamics of Stardust Sample Return Capsule. *Journal of Spacecraft and Rockets*, 36:436–441, 1999.

[17] H. Alkandry, I. D. Boyd, and A. Martin. Comparison of Models for Mixture Transport Properties for Numerical Simulations of Ablative Heat-Shields. In *51st AIAA Aerospace Sciences Meeting Including the New Horizons Forum and Aerospace Exposition*, 2013.

[18] E. Fahy, R. J. Gollan, D. R. Buttsworth, P. A. Jacobs, and R. G. Morgan. Expansion Tube and Computational Fluid Dynamics Studies of Superorbital Earth Re-entry. In *46th AIAA Thermophysics Conference*, 2016.

[19] B. Lopez and M. Lino da Silva. SPARK : A Software Package for Aerodynamics , Radiation and Kinetics. In *46th AIAA Thermophysics Conference*, 2016.

[20] L. C. Scalabrin and I. D. Boyd. Numerical Simulations of the FIRE-II Convective and Radiative Heating Rates. In *39th AIAA Thermophysics Conference*, 2007.

[21] C. Park. Stagnation-Point Radiation for Apollo 4. *Journal of Thermophysics and Heat Transfer*, 18: 349–357, 2004.

[22] V. Carandente, R. Savino, M. Iacovazzo, and C. Boffa. Aerothermal Analysis of a Sample-Return Reentry Capsule. *Fluid Dynamics and Materials Processing*, 9:461–484, 2013.

[23] J. D. Anderson. *Hypersonic and High Temperature Gas Dynamics*. AIAA, 1989.

[24] B. Lopez. *Simulation des Écoulements de Plasma Hypersonique Hors Équilibre Thermochimique*. PhD thesis, Université D'Orléans, 2010.

[25] C. Park, R. L. Jaffe, and H. Partridge. Chemical-Kinetic Parameters of Hyperbolic Earth Entry. *Journal of Thermophysics and Heat Transfer*, 15:76–90, 2001.

[26] B. Lopez, M. Lino da Silva, V. Guerra, and J. Loureiro. Coupled Hydrodynamic / State-Specific High-Temperature Modeling of Nitrogen Vibrational Excitation and Dissociation. In *44th AIAA Thermophysics Conference*, 2013.

[27] G. G. Chernyi, S. A. Losev, S. O. Macharet, and B. V. Potapkin. *Physical and Chemical Processes in Gas Dynamics: Cross Sections and Rate Constants*. AIAA, 2002.

[28] G. G. Chernyi, S. A. Losev, S. O. Macharet, and B. V. Potapkin. *Physical and Chemical Processes in Gas Dynamics: Physical and Chemical Kinetics and Thermodynamics of Gases and Plasmas*. AIAA, 2004.

[29] C. Park. Assessment of Two-Temperature Kinetic Model for Ionizing Air. *Journal of Thermophysics and Heat Transfer*, 3:233–244, 1989.

[30] R. C. Millikan and D. R. White. Systematics of Vibrational Relaxation. *The Journal of Chemical Physics*, 39:3209–3213, 1963.

[31] J. S. Shang and S. T. Surzhikov. Nonequilibrium radiative hypersonic flow simulation. *Progress in Aerospace Sciences*, 53:46–65, 2012.

[32] S. Chapman and T. G. Cowling. *The Mathematical Theory of Non-Uniform Gases*. Press Syndicate of the University of Cambridge, 1990.

[33] C. R. Wilke. A Viscosity Equation for Gas Mixtures. *The Journal of Chemical Physics*, 18:517–519, 1950.

[34] G. E. Palmer and M. J. Wright. Comparison of Methods to Compute High-Temperature Gas Viscosity. *Journal of Thermophysics and Heat Transfer*, 17:232–239, 2003.

[35] F. G. Blottner, M. Johnson, and M. Ellis. Chemically Reacting Viscous Flow Program for Multi-Component Gas Mixtures. Technical report, Sandia Laboratories, 1971.

[36] W. G. Vincenti and C. H. Kruger. *Introduction to Physical Gas Dynamics*. Krieger Publishing Company, 2002.

[37] P. Gnoffo, R. N. Gupta, and J. L. Shinn. Conservation Equations and Physical Models for Hypersonic Air Flows in Thermal and Chemical Nonequilibrium. Technical report, NASA, 1989.

[38] R. N. Gupta, J. M. Yos, and R. A. Thompson. A Review of Reaction Rates and Thermodynamic and Transport Properties for the 11-species Air Model for Chemical and Thermal Nonequilibrium Calculations to 30000 K. Technical report, NASA, 1990.

[39] F. F. Chen. *Introduction To Plasma Physics and Controlled Fusion*, volume 1. Plenum Press, 1984.

[40] J. H. Lee. Basic Governing Equations for the Flight Regimes of Aeroassisted Orbital Transfer Vehicles. In *AIAA 19th Thermophysics Conference*, 1984.

[41] K. Sutton and R. A. Graves. A General Stagnation-Point Convective-Heating Equation for Arbitrary Gas Mixtures. Technical report, NASA, 1971.

[42] M. E. Tauber and K. Sutton. Stagnation-Point Radiative Heating Relations for Earth and Mars Entries. *Journal of Spacecraft and Rockets*, 28:40–42, 1990.

[43] R. K. Agarwal, K. Yun, and R. Balakrishnan. Beyond Navier-Stokes: Burnett equations for flows in the continuum-transition regime. *Physics of Fluids*, 13:3061–3085, 2001.

[44] D. D. Loureiro. High-Temperature Modeling of Transport Properties in Hypersonic Flows. Master's thesis, Instituto Superior Técnico, 2015.

[45] R. W. MacCormack. Carbuncle Computational Fluid Dynamics Problem for Blunt-Body Flows. *Journal of Aerospace Information Systems*, 10:229–239, 2013.

Appendix A

RAM-C II at 10 km/s

Figure A.1 shows the profiles for (a) stagnation line temperature and (b) wall heat flux considering the RAM-C II geometry and a reentry velocity of 10 km/s. The mesh considered was the one used by Loureiro [44]. The initial conditions are the same for point 3 of Trajectory 15.9.

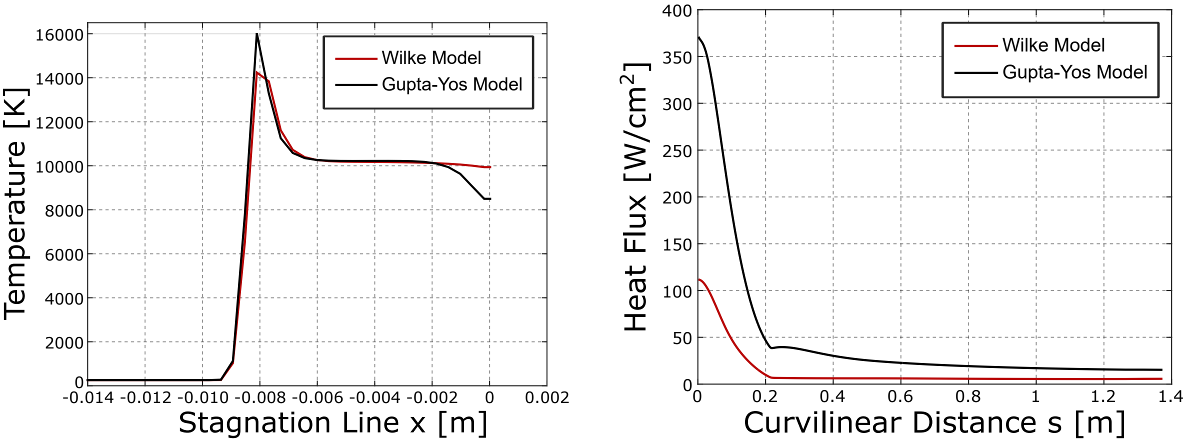

(a) Stagnation Line Temperature

(b) Wall Heat Flux

Figure A.1: Profiles for (a) stagnation line temperature and (b) wall heat flux considering the RAM-C II geometry and a reentry velocity of 10 km/s for both transport models.

Comparing these results to the ones obtained considering the initial conditions used by Loureiro [44], the considered reentry velocity greatly impacts the temperature and wall heat flux profiles. The results shown in Fig. A.1 present a higher peak temperature value and a temperature constant region. Moreover, it is verified that the impact of the transport model on the wall heat fluxes, is greater at higher velocities. These results validate the discussion in section 4.1.

Appendix B

Poster

A poster describing this work was presented at HyMEP - Hypersonic Meteoroid Entry Physics - 61st Course of the International School of Quantum Electronics, 2017, in Erice, Sicily.

corresponding authors:
marta.bruxelas@tecnico.ulisboa.pt
maria.castela@tecnico.ulisboa.pt
mlinodasilva@tecnico.ulisboa.pt
belopez@illinois.edu

DIVER - From A to Z, Design of a Reentry Vehicle for Phobos Sample Return Mission

M. Bruxelas[1], M. Castela[1], B. Lopez[1,2], M. Lino da Silva[1]

[1] Instituto de Plasmas e Fusão Nuclear, Instituto Superior Técnico, Universidade de Lisboa, Lisbon, Portugal
[2]University of Illinois at Urbana-Champaign, Urbana, IL 61801, USA

Introduction

Phobos Sample Return Mission was designed to collect samples from the Martian moon Phobos and returning them to Earth. This mission is a first step towards manned missions to Mars. Accurate assessement of the heat fluxes during the high speed, hyperbolic reentry is critical to the overall spacecraft design. The impact of the reentry flow conditions on the capsule is evaluated here by means of CFD simulations.

DIVER is a Portuguese consortium project comprising Spin.works, INEGI, IST-DEM and IPFN, funded by Portugal2020. It gathers all the concurrent engineering required in the preliminary design of a reentry vehicle in the Phobos sample return mission. Two trajectories for the capsule descent are considered, one with a flight path angle (fpa) of -15.9º and the other with fpa = -24.2º. In both trajectories, the maximum value of the reentry velocity is 11.6km/s.

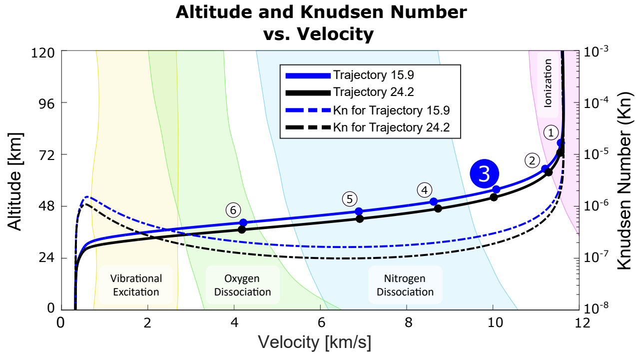

Figure 1. Different phenomena taking place along both trajectories and simulation points.

Engineering models held a first estimation of the aerodynamic coefficients and heat fluxes on the forward body. These estimations are then complemented by CFD simulations in **key trajectory points**: peak convective heating - point 3 and peak decelerating heating - point 5.

Velocity [km/s]	Altitude [km]	Density [g/m^3]
10.07	55.81	0.486
Temperature [K]	Pressure [Pa]	Kn
257.18	35.90	0.26

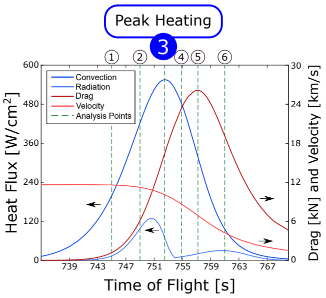

Figure 2. Application of correlations for simulation point selection. (Courtesy of Spin.works)

Software Package for Aerodynamics Radiation and Kinetics

SPARK aims at improving the prediction capability of numerical simulations of hypersonic reentry flows [1].

Two distinct classes of physical models are implemented in SPARK, **multi-temperature models** or **state-specific description**.

- ➔ SPARK is able to **compute multi-dimensional simulations** using a **state-specific kinetic model**.
- ➔ We are working on **SPARK code optimization** to explore the near-future **EXASCALE computing resources**.

Geometry and Numerical Setup

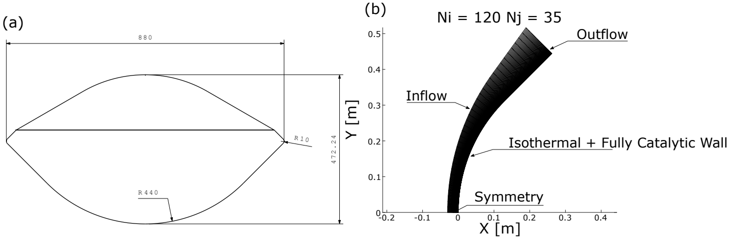

Figure 3. (a) Capsule geometry and (b) Computational mesh and boundary conditions.

Two **geometries** were considered, one identical to the Hayabusa capsule, and a another shown in Fig. 3(a). Figure 3(b) shows the **mesh** considered for the simulations, where Ni is the number of elements along the stagnation line and Nj the elements along the capsule surface. It consists of 4200 elements.

Results

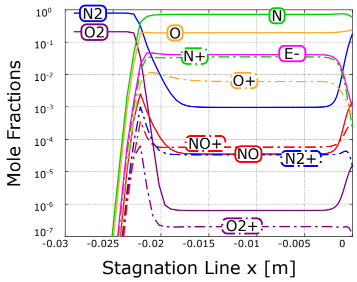

Stagnation Line x [m]

Figure 4. Mole fractions along the stagnation line.

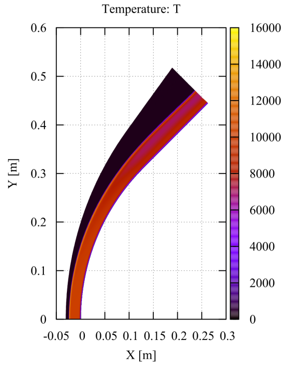

Figure 5. 2D Temperature field.

Different Transport Models / Reentry Velocities

V = 10 km/s

Present Work

V = 6 km/s

RAM-C II [2]

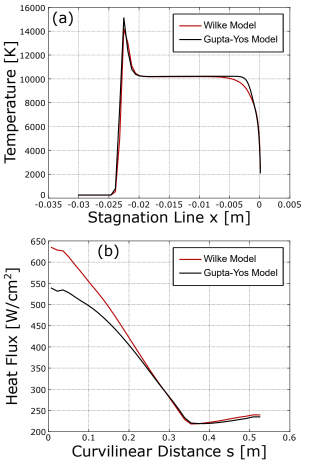

Figure 6. (a) Temperature along the stagnation line and (b) heat flux along the capsule surface computed with Wilke and Gupta-Yos transport models.

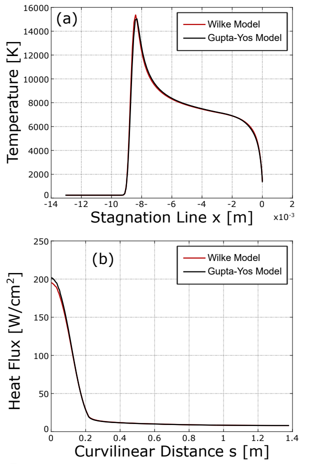

Figure 7. (a) Temperature along the stagnation line and (b) heat flux along the capsule surface computed with Wilke and Gupta-Yos transport models.

- ➔ The **temperature peak** is similar for both velocities. For lower velocities, the temperature does **not stabilize** along the shock layer, as it does for higher velocities.
- ➔ The selection of the **transport model** has a **higher impact** on the results for **higher velocities**. Wilke model **overestimates** the wall heat flux by 19% when compared to the Gupta-Yos model, for these conditions.

Future work includes radiation computation.

References

[1] B. Lopez and M. Lino da Silva, 46th AIAA Thermophysics Conference, 13-17 June 2016, Washington, D.C, 2016-4025.

[2] D. Loureiro, *High-Temperature Modeling of Transport Properties in Hypersonic Flows*, MSc Thesis, Instituto Superior Técnico, Lisboa, 2015.

Aknowledgements

IPFN activities received finantial support from Fundação para a Ciência e Tecnologia through project UID/FIS/50010/2013. This work has been funded by POCI-01-0247-FEDER-003476.